Elsevier Editorial System(tm) for Precambrian Research
Manuscript Draft

Manuscript Number:

Title: The P-T-t architecture of a Gondwanan suture: REE, U-Pb and Ti-in-zircon thermometric constraints from the Palghat Cauvery shear system, South India

Article Type: Research Paper

Section/Category:

Keywords: Gondwana; UHT metamorphism; Monazite; Zircon; Garnet; THERMOCALC

Corresponding Author: Dr. Chris Clark,

Corresponding Author's Institution: Curtin University

First Author: Chris Clark

Order of Authors: Chris Clark; Alan S Collins; M Santosh; Richard Taylor; Benjamin Wade

Manuscript Region of Origin:

Abstract: Understanding the relationship between accessory mineral growth and the evolution of silicate mineral assemblages along the entirety of a P-T-t path is a critical step in developing models for evolving tectonic systems. Here we combine U-Pb age data (for zircon and monazite), rare earth element (REE) data and compositionally specific phase diagrams (P-T pseudosections) for the rocks of the Palghat Cauvery shear system (PCSS), southern India in order to constrain the periodicity of heating /cooling and burial/exhumation events during the Ediacaran/Cambrian amalgamation of Gondwana. HREE data from zircon is consistent with zircon growth at 672-724 °C during the breakdown of garnet in the kyanite stability field at 535.0 ± 4.9 Ma. This represents a cooling that punctuates the P-T-t path. Subsequent monazite growth and symplectite formation occurred at 920 °C and 7.5 kbar, ~10 Ma after zircon growth which reflects a period of reheating and decompression related to delamination and the collapse of the East African orogen. The REE chemistry of the monazite is consistent with the system having undergone partial melting prior to monazite growth, thereby altering the bulk rock chemistry. The periodicity of the heating and cooling cycles (~10 Ma) from this study are consistent with recently proposed tectonic switching models for the formation of granulite metamorphism in accretionary/collisional tectonic settings. The elevated heat flows required to generate the UHT metamorphism are achievable in the proposed back-arc setting for the PCSS during Gondwana amalgamation.

The *P-T-t* architecture of a Gondwanan suture: REE, U-Pb and Ti-in-zircon thermometric constraints from the Palghat Cauvery shear system, South India

Chris Clark[1*], Alan S. Collins[2], M. Santosh[3], Rich Taylor[4], Benjamin P. Wade[2]

[1]The Institute for Geoscience Research (TIGeR), Department of Applied Geology, Curtin University of Technology, GPO Box 1987, Perth WA 6845, Australia

[2]Tectonics and Resource Exploration (TREx), School of Earth & Environmental Sciences, University of Adelaide, 5005, Australia.

[3]Faculty of Science, Kochi University, Akebono-cho 2-5-1, Kochi 780-8520, Japan

[4]Grant Institute of Earth Science, School of GeoSciences, University of Edinburgh, Kings Buildings, West Mains Rd, Edinburgh, EH9 3JW Scotland

Abstract

Understanding the relationship between accessory mineral growth and the evolution of silicate mineral assemblages along the entirety of a *P-T-t* path is a critical step in developing models for evolving tectonic systems. Here we combine U-Pb age data (for zircon and monazite), rare earth element (REE) data and compositionally specific phase diagrams (*P-T* pseudosections) for the rocks of the Palghat Cauvery shear system (PCSS), southern India in order to constrain the periodicity of heating /cooling and burial/exhumation events during the Ediacaran/Cambrian amalgamation of Gondwana. HREE data from zircon is consistent with zircon growth at 672-724 °C during the breakdown of garnet in the kyanite stability field at 535.0 ± 4.9 Ma. This represents a cooling that punctuates the P-T-t path. Subsequent monazite growth and symplectite formation occurred at 920 °C and 7.5 kbar, ~10 Ma after zircon growth which reflects a period of reheating and decompression related to delamination and the collapse of the East African orogen. The REE chemistry of the monazite is consistent with the system having undergone partial melting prior to monazite growth, thereby altering the bulk rock chemistry. The periodicity of the heating and cooling cycles (~10 Ma) from this study are consistent with recently proposed tectonic switching models for the formation of granulite metamorphism in accretionary/collisional tectonic settings. The elevated heat flows required to generate the UHT metamorphism are achievable in the proposed back-arc setting for the PCSS during Gondwana amalgamation.

Keywords: Gondwana; UHT metamorphism; Monazite; Zircon; Garnet; THERMOCALC

Introduction

The integration of the textural and chemical characteristics of accessory and silicate minerals provides invaluable information when investigating the metamorphic and tectonic history of a terrane (e.g. Buick et al., 2006; Hermann and Rubatto, 2003; Kelsey et al., 2007; Rubatto, 2002; Rubatto and Hermann, 2007; Rubatto et al., 2006; Rubatto et al., 2001; Whitehouse and Platt, 2003). In particular, the information extracted from mineral assemblages can be used to great effect in making inferences about poorly understood processes such as those involved in the generation, preservation and tectonic significance of ultrahigh temperature (UHT) metamorphic assemblages (Harley, 1998a; Harley, 1998b; Harley and Kelly, 2007; Kelly and Harley, 2005). Coupling these observations with calculated metamorphic phase diagrams for specific equilibrium bulk rock compositions (*P*-*T* pseudosections) allows a clearer picture of the whole *P*-*T*-*t* evolution of a terrane to be reconstructed (e.g. Clark et al 2007; Kelsey et al., 2007). This approach is especially important in terranes that have undergone UHT metamorphism due to the uncertainty surrounding the ability of geochronometers to record the timing of peak metamorphism (Fraser et al., 1997; Harley, 2004; Kelsey et al., 2008; Roberts and Finger, 1997; Tomkins et al., 2005). This uncertainty reflects (1) the lack of absolute knowledge regarding closure temperature and rates of elemental diffusion in key geochronometers such as zircon and monazite and (2) the lack of certainty as to the exact controls on the growth of zircon and monazite and how it relates to mineral reactions above and below the solidus. Recent advances in the application of accessory phase thermometry (e.g. Watson and Harrison, 2005; Watson et al., 2006; Ferry and Watson, 2007) allows constraints to be placed on the temperatures at which accessory phase growth occurred. This information can then be incorporated with the metamorphic forward models allowing a detailed event chronology, linking textural, temporal and thermal observations, to be constructed. It is only when this information is gathered that insights into the tectonic processes that created the metamorphism are generated and the significance of the nature and timing of metamorphism for plate-tectonic global reconstructions (e.g. Boger and Wilson, 2005; Collins and Pisarevsky, 2005; Li et al., 2007) can be addressed.

In this paper we investigate the major and trace element compositions of garnet, zircon and monazite in order to constrain the timing and rates of processes in the Palghat Cauvery shear system (PCSS) in southern India (Fig. 1). This region preserves a distinctive record of high-grade metamorphism coupled with accessory mineral development and is a key area in understanding the tectonic scenarios that may lead to the generation of ultra-high temperature crustal metamorphism. There is also a recent debate surrounding the report of eclogite facies rocks from this area (Kelsey et al., 2006; Shimpo et al., 2006; Tsunogae and Santosh, 2006; Kanazawa et al., 2009) and the significance that these rocks have in defining the location of major suture/collision zones during the amalgamation of Gondwana (Collins et al., 2007b; Collins and Pisarevsky, 2005).

Regional Geology

The PCSS is an approximately 70 km by 400 km E-W zone characterised by an anastomosing network of mainly dextral shear zones, typically 1-10km wide, separating the Dharwar Craton from the Southern Granulite Terrane (SGT) in southern India. (Chetty et al., 2003; Tomson et al., 2006) (Fig.1). The lithologies within the PCSS consist of deformed Neoarchaean rocks; variably retrograded charnockitic gneisses associated with biotite and hornblende-bearing migmatitic gneisses intercalated with supracrustal rocks that include, metapelites, calc-silicate marbles and quartzites (Bhaskar Rao et al., 1996; Chetty and Bhaskar Rao, 2006).

A number of previous studies have found significant differences in the structural style, lithological units, Nd model ages, Rb-Sr mineral ages and metamorphic *P-T* conditions of the lithologies within the PCSS when compared to the Dharwar Craton and SGT (Bartlett et al., 1998; Ghosh et al., 2004; Harris et al., 1994b; Meissner et al., 2002; Santosh et al., 2005; Santosh et al., 2003). As a result the PCSS has been proposed to represent a major structural feature within southern India. The PCSS has been interpreted as (1) a dextral transcurrent shear belt (Drury et al., 1984); (2) a suture zone (Bhaskar Rao et al., 2003; Meissner et al., 2002); (3) an Archaean-Palaeoproterozoic terrane boundary (Harris et al., 1994b); (4) a collapsed marginal basin (Drury and Holt, 1980) and (5) a zone of Palaeoproterozoic and Neoproterozoic re-working of Archaean crust (Bhaskar Rao et al., 1996; Chetty et al., 2003; Ghosh et al., 2004; Harris et al., 1994b; Santosh et al., 2003; Tomson et al., 2006). The notion that the PCSS represents the Archaean-Proterozoic or Neoproterozoic terrane boundary has been contested, based on new U-Pb zircon age data and Sm-Nd model ages for charnockitic and migmatitic gneisses (Bhaskar Rao et al., 2003; Ghosh et al., 2004). These studies suggest that the Archaean crust may extend south of the PCSZ up to Karur-Kamban-Painavu-Trichur (KKPT) shear zone (Ghosh et al., 2004) (Fig. 1).

In tight-fit reconstructions of Gondwana, southern India is juxtaposed against Madagascar and East Antarctica (Reeves and de Wit, 2000), where the major suture zones of the amalgamation of eastern Gondwana have been identified and correlated through adjoining crustal blocks (Boger and Miller, 2004; Collins et al., 2007b; Collins and Pisarevsky, 2005; Fitzsimons, 2000; Meert, 2003; Meert and Van der Voo, 1997; Shaju et al., 1998). A number of different microcontinents have been identified within the models of the amalgamation of eastern Gondwana; the most significant of which, in the context of southern India, is Azania – a microcontinent consisting of central Madagascar, part of eastern Africa and the Al-Mafid Block in Yemen (Collins and Pisarevsky, 2005; Collins et al., 2007a). Prior to the formation of Gondwana, the Mozambique Ocean was located between Azania and India. The closure of the Mozambique Ocean formed the ~550-510 Ma Malagasy Orogeny (Collins and Pisarevsky, 2005). The site of this closure has been identified in eastern Madagascar as the Betsimisaraka suture (Collins, 2006; Collins and Windley, 2002), but its southern continuation is contentious. Recent work has demonstrated that the PCSS marks an isotopic boundary between the Northern Granulite and Southern Granulite terranes (Clark et al., 2009; Fig 1), contains discontinuous ultramafic bodies that are coincident with crust penetrating shear zones that offset the Moho (Collins et al., 2007b; Meissner et al., 2002) and may contain evidence of Neoproterozoic UHP metamorphism (Shimpo et al., 2006) and therefore is a likely candidate for the continuation of the Betsimisaraka suture into southern India.

Results

Petrography

Sample description

The petrology of the various units that occur in the Panagad area have been investigated in detail by Kanazawa et al. (2009) and this study we have focussed on one lithology type a garnet-kyanite-biotite gneiss, sample I05-54. I05-54 is from an Mg-Al rich granulite from Panangad within the PCSS (Fig. 1b). This Mg-Al rich unit occurs as a 10 to 50 metre wide unit that is discordant with the migmatitic layering in the host mafic gneisses. The unit shows a general north-easterly trend with a steep (>75°) northwest dip and a near vertical lineation defined by alignment of kyanite (Fig 2a). The unit has a variable mineralogy with garnet, kyanite, biotite, gedrite, sapphirine and cordierite all visible in within the unit (see Kanawazaet al., (in press) for further details). Sample I05-54 is composed of coarse-grained garnet, kyanite and biotite with sapphirine is observed rimming the kyanite blades whereas cordierite and gedrite are not visible in hand sample (Fig. 2b).

In thin section, I05-54 displays three distinct petrographic relationships: (1) an inclusion rich garnet core (Fig. 2c); (2) a coarse grained garnet, kyanite and biotite assemblage, and (3); symplectite development between the coarse-grained minerals (Fig. 2d).

Inclusion assemblage

Coarse grained garnets contain a zone rich in inclusions (Fig 2c). Inclusions are restricted to the core of the garnets and are completely enclosed by a clean inclusion free garnet rim. The inclusions are dominantly gedrite, sillimanite, and quartz (Fig. 2e) with minor plagioclase observed in some inclusions. The stability of this inclusion assemblage with garnet is difficult to assess. Vernon (1976) suggests that in general most inclusions belong to the same metamorphic assemblage as the porphyroblast. However, the inclusion assemblage may have formed prior to garnet growth as gedrite and quartz are only found as inclusions within garnet and not elsewhere in the rock

(Vernon et al., 2008). Accessory minerals observed in the garnet cores are rutile, zircon, monazite and apatite. Zircon within the garnet is dominantly oscillatory zoned with overgrowths either narrow or absent. Zircon occurs as oscillatory-zoned grains with an absence of any discernable rim or overgrowth material visible under cathodoluminscence (CL). Collins et al. (2007b) analysed the oscillatory zoned zircon from this sample and found that the age of oscillatory zoned zircon was ~2500 Ma. This population is interpreted to be of igneous origin and inherited from the source material that makes up the bulk of the gneisses in the PCSS. Monazite from within the core of the garnets is small with grain sizes generally less than 20 μm.

Coarse-grained assemblage

I05-54 is dominated by porphyroblastic garnet, kyanite and biotite. As mentioned above, garnet is characterised by an inclusion-rich core and an inclusion-free rim. Biotite is coarse grained and contains rare inclusions of zircon, the zircons have well developed overgrowths on oscillatory zoned cores. Kyanite blades are partly pseudomorphed by sillimanite with kyanite remaining in the core and more highly birefringent sillimanite forming on the rims. Kyanite contains inclusions of both rutile and zircon (Fig. 2f) with zircon having well-developed overgrowths. A single xenotime crystal was observed in the otherwise inclusion free garnet rim (Fig. 3g)

Symplectites

Sapphirine-cordierite and spinel-cordierite symplectites are observed growing between garnet and kyanite porphyroblasts with cordierite separating garnet from sapphirine and spinel (Fig. 2g). In places sapphirine-spinel-cordierite symplectites have developed between the porphyroblastic kyanite and biotite. Additionally a narrow cordierite corona separates the garnet from the biotite without the additional growth of sapphirine or spinel. Where garnet, kyanite and biotite are all proximal, a cordierite-spinel-sapphirine-biotite symplectite is formed with the biotite being fine-grained, bladed and in contact with the garnet (Fig. 2h). The dominant accessory phase observed in the symplectites is monazite, which is intergrown with both the sapphirine-cordierite and the spinel-cordierite symplectites (Fig. 2i). In contrast to the monazite found in the cores of the garnet, the monazite in the symplectite is typically large (>50 μm). Smaller grains of xenotime are also found in the symplectites (Fig. 3g).

Mineral chemistry

Mineral compositions were analysed using the Cameca SX-51 electron microprobe at Adelaide Microscopy at The University of Adelaide. Quantitative analyses for mineral chemistry were acquired at 15 kV and 20 nA and a beam diameter of 2-3 *μ*m, Compositional maps were acquired at 15 kV and 100 nA for major elements (Figs. 3a-d) and 150 nA for trace elements (Figs. 3e-g) with a ‘dwell time’ of 195 ms and a step-size of 2 μm in both the x and y directions. A summary of the analyses can be found in Tables 1 and 2.

Garnet

Porphyroblastic garnet is in generally a solid solution of almandine and pyrope with X_{Mg} (=Mg/Fe+Mg) in the range of 0.51-0.62 (Table 1) with low contents of grossular (<3 mol %) and spessartine (<1.15 mol%). Garnet has shows a pyrope rich core (Alm_{36-39} Pyr_{58-61} Sps_1 Grs_{1-3}) relative to the rim (Alm_{42-44} Pyr_{49-51} Sps_1 Grs_{1-3}) consistent with retrograde diffusion and the occurrence of the cordierite coronae around the garnet (Table 1; Fig 3a-d). The compositional zoning of the major elements is also evident in the electron microprobe traverse presented in Figure 4a.

Biotite

Biotite is Mg rich (X_{Mg}=0.80-0.81) and contains approximately 2 wt% TiO_2 (Table 2). Both the coarse grained and symplectitic biotite have similar compositions.

Cordierite

All cordierite analyses have a uniform magnesian composition with X_{Mg} in the range 0.89-0.91 (Table 2).

Sapphirine

The symplectitic sapphirine is less magnesian (X_{Mg}= 0.76-0.78, Table 2) compared to other studies from the PCSS (Koshimoto et al., 2004; Santosh and Sajeev, 2006; Santosh et al., 2004; Shimpo et al., 2006). Other components apart from SiO_2 (11.7-12.3 wt%) and Al_2O_3 (61.1-62.5 wt%) total less than 1 wt%.

Gedrite

As previously mentioned gedrite only occurs as inclusions within the cores of the porphroblastic garnet and is associated with quartz and sillimanite. The gedrite inclusions preserve an X_{Mg} range of 0.77-0.78. The Na_2O content ranges from 1.28-1.62 wt% and TiO_2 show a range of 0.26-0.46 wt%.

Spinel

Symplectitic spinel occurs in association with cordierite is principally a solid solution of hercynite and Mg-spinel with consistent X_{Mg} values of 0.46-0.47 (Table S2). Spinel also contains a small amount of Cr_2O_3 (0.33-0.51 wt%) and ZnO (0.80-1.20 wt%).

Zircon and Monazite geochronology

Equipment and operating conditions for monazite analysis are identical to those reported by Payne et al (2008). U-Pb acquisition used a 15 μm beam diameter for monazite, run at a repetition rate of 5 Hz. Monazite ages were calculated using the MADEL monazite standard to correct for U-Pb fractionation (TIMS normalization data $^{207}Pb/^{206}Pb$ = 490.7 Ma, $^{206}Pb/^{238}U$= 514.8 Ma and $^{207}Pb/^{235}U$= 510.4 Ma), and the GLITTER software for data reduction. Over the duration of this study the reported average normalised ages for MADEL are 493.0±8.3, 514.3±2.4 and 511.2±2.0 Ma for the $^{207}Pb/^{206}Pb$, $^{206}Pb/^{238}U$ and $^{207}Pb/^{235}U$ ratios, respectively (n = 32). Accuracy was monitored by repeat analyses of the in-house internal monazite standard (94-222/Bruna-NW, $^{206}Pb/^{238}U$= 447 Ma). Over the duration of this study the reported average $^{206}Pb/^{238}U$ age for the internal standard was 446.9±3.1 (n = 15). Analytical data for the analyses can be found in Tables 6.

Zircon and monazite were separated from crushed rock samples by conventional magnetic and methylene iodide liquid separation methods. Grains were handpicked and mounted in epoxy resin discs. No grains of monazite less than 50 μm in diameter analysed in an attempt to avoid the analysis of the monazite inclusions from the garnet cores. The grains were cathodoluminescence (CL) imaged (zircon) or backscatter electron (BSE) imaged (monazite) to assess compositional and textural zoning in individual grains prior to analysis. Multi-faceted equant zircon crystals (Fig. 5a) and large brightly luminescent CL rims (Fig. 5b-d) yielded a precise $^{206}Pb/^{238}U$ age of 535.0 ± 4.9 Ma (2σ, MSWD = 1.4, Fig. 5e) and Th/U ratios from these analyses are <0.22, characteristic of metamorphic zircon. The details of these data are presented in Collins et al. (2007) The LA-ICPMS analyses of monazite yielded two statistically distinct ages, the cores (Fig.6a) of monazite yielded a $^{206}Pb/^{238}U$ age of 525.7 ± 3.9 Ma (2σ, MSWD = 0.17, Fig. 6b, Table 3) whereas overgrowths (Fig. 6a) on the monazite cores gave a $^{206}Pb/^{238}U$ age of 515.7 ± 4.7 (2σ, MSWD = 0.20, Fig 6c, Table 3).

Garnet, zircon, monazite trace element chemistry

Rare Earth Element (REE) compositions of minerals (Table 4, 5 and 6) were performed by laser ablation inductively coupled mass-spectrometry (LA-ICPMS) on block mounted mineral separates at The University of Adelaide using a Agilent 7500cs ICPMS equipped with a New Wave 213 nm Nd-YAG laser. Beam diameter was set at 65μm using a repetition rate of 5 Hz which produced a laser power density of ~14-16 J cm^{-2}. Data was collected using time-resolved data acquisition in fast peak-jumping mode and processed using the GLITTER software (Van Achterbergh et al., 2001). Total acquisition time per analysis was 120 seconds; 60 seconds background measurement followed by 60 seconds of sample ablation. Calibration was performed against the NIST 612 standard glass using the coefficients of Pearce et al. (1997). NIST was run 4 times at the beginning and end of a run, interspersed by two analyses of BCR-2 and ten analyses of unknowns. ^{43}Ca was used as the internal standard for garnet and monazite and Si for zircon, applying previously determined values from microprobe analysis. Precision based on repeated analyses of standards is approximately ±10% for concentrations <10ppm. Typical detection limits for REE in this study ranged from 0.04-0.6 ppm.

Ti in zircon was measured in the same analytical run as the REE analyses. The less abundant ^{49}Ti isotope (5.41%) was analysed in preference to the more abundant ^{48}Ti isotope (73.72%) to avoid the interference with ^{96}Zr. Individual temperature errors (Table 5) are a function of counting statistics, standard calibration and the uncertainty in the thermometer calibration and were calculated via propagation of the 2σ errors of the counting statistics and the standard calibration through the Ti in zircon thermometer of Watson and Harrison (2006).

Garnet

The trace element distribution in garnet from I05-54 was analysed by a LA-ICPMS traverse (Fig. 4a) and electron probe compositional mapping (Fig. 3e-g). The LA-ICPMS traverse consisted of 17 spot analyses across a garnet with a diameter of approximately 6000 μm (Fig. 3a). Zoning is observed in a number of the trace elements with a few different patterns being recognised. As described earlier, the garnet consists of two main zones, the inclusion rich core and the inclusion free rim, and most of the elemental zoning patterns observed in the maps and the LA-ICPMS traverse reflect a change associated with the transition between the two garnet types.

Garnet maps show zoning in P (Fig 3f) with the garnet core more depleted (6-70 ppm) relative to the rim (159-266 ppm) with a step increase at the transition between the core and rim. This pattern is similar to the patterns observed for Zr and Hf (Table 4). The core of the garnet is contains 43-85 ppm Y, 3-11 ppm Yb and .3-1.3 ppm Lu. The

HREE-poor core then transitions in to an intermediate domain with Y contents 105-135 ppm, 16-32 ppm Yb and and 2.2-6 ppm Lu with a corresponding increases in the other HREE, Co, and Ni. The beginning of the intermediate Y rich zone also represents the largest drop in Sc, Ti and V (184-223 ppm Sc, 69-77 ppm Ti and 67-74 ppm V in the core), which then gradually decrease rimward (61-158 ppm Sc, 32-55 Ti ppm and 24-49 ppm V from the intermediate zone to rim) in there abundances. Y, Co, Ni and the HREE then show a decrease in their relative elemental abundances back to those measured in the core moving towards the rim of the garnet.

In summary three main zoning styles are observed in the trace elements of the garnets. These are:

(1) A bell shaped zoning pattern in the Sc, Ti and V with a step decrease in abundance that corresponds with the petrographically observed core/rim transition in the garnet;

(2) A W-shaped trend in P, Zr and Hf with core and rims relatively enriched in these elements relative to the intermediate area, although the elements are much more strongly enriched in the rims than in the core, and;

(3) A zoning pattern that consists of a low abundance flat core, near symmetric peaks corresponding with the petrographically observed core/rim transition that drop off toward the rims. This pattern is observed in Co, Ni, Y and the HREE from Gd to Lu with the pattern becoming more pronounced moving from Gd to Lu.

Garnet chondrite-normalised REE patterns for sample I05-54 show similar features that are common to high-grade garnet in granulite terranes (Degeling et al., 2001; Harley and Kelly, 2007; Harley et al., 2007; Hermann and Rubatto, 2003; Kelly and Harley, 2005; Whitehouse and Platt, 2003) with one major exception. This exception is that there is no significant Eu anomaly (Eu/Eu* 0.80-1.05) associated with the garnet in any of the textural zones described earlier. However, the garnet displays a consistent depletion in the LREE with all well below chondrite values and enrichment in the HREE relative to chondrite. Variation in the relative HREE enrichment in the textural domains is observed across the garnet (Fig. 4c). The garnet core is more depleted (Fig. 4, Lu/Gd 0.09-0.19) relative to a more enriched intermediate zone (Fig. 4, Lu/Gd >1.0) that corresponds to the interface between the core and rim of the garnet. The HREE content is depleted from this more enriched zone towards the rim (Fig. 4, Lu/Gd 0.17-0.65). The relative abundance of the LREEs remains constant across the garnet.

Zircon

All zircon analysed from the sample occurred as either multi-faceted equant zircon crystals (Fig.5a) or as wide, brightly luminescent, under CL, overgrowths on oscillatory-zoned cores (Fig. 5b-d). Once again the patterns are similar to those found in zircons from high-grade metamorphic rocks, particularly those inferred to have formed in sub-solidus conditions (Hoskin and Schaltegger, 2003; Rubatto, 2002), with flat to slightly negative HREE patterns (Lu/Gd 0.11-0.18) positive Ce anomalies (Ce/Ce* 12-74), and no negative Eu anomalies (Eu/Eu* 0.89-1.01). The LREE elements are close to, or below, chondrite values. The Th/U ratios obtained from the analysed zircon were in the range 0.09-0.22 (Collins et al., 2007), this is consistent with the zircon growth occurring during metamorphism (Corfu et al., 2003; Williams and Claesson, 1987). The REE composition of the oscillatory zoned cores that yielded Archaean ages was analysed and found to have distinctly different chondrite normalised REE patterns (Fig. 5g) with much steeped HREE slopes than the unzoned c. 535 Ma population.

The Ti contents of the zircons were also analysed in order to constrain the temperature at which the zircons grew. Due to the large beam size of the laser and the relative width of zircon overgrowths no trends in the data was able to be detected, i.e. zoning from high temperature early growth to low temperature later rim growth, was able to be detected. The measured Ti values ranged between 4.3-11.7 ppm (Table 5) which corresponds to a temperature range of 672-724 °C using the Ti in zircon thermometer (Fig. 4f; Watson and Harrison, 2005; Watson et al., 2006). The application of the Ti in zircon thermometer is dependent on the growth of zircon in equilibrium with a suitable buffering assemblage of quartz and rutile (Ferry and Watson, 2007), while these minerals are present in the rock it cannot be assumed that they are in equilibrium. The reasons why they are believed to be in equilibrium will be discussed in the next section.

Monazite

Monazite data for sample I05-54 are plotted on Fig 6d and presented in Table 6. Due to the analytical spot size (65 μm) only the core regions of monazite was analysed as the overgrowths were to narrow. The trace element pattern, when normalised against chondrite, shows a strong relative enrichment in the LREE (232 000- 540 000 times chondrite for La) with a smooth decrease in the normalised abundance towards the HREE (Fig. 6d). The monazite from I05-54 displays a small negative Eu anomaly (Eu/Eu* 0.60-0.78) (Fig 6d).

Discussion

Garnet zoning and zircon chemistry

The notion that the trace element composition of zircon and garnet can be used to correlate growth events between these minerals is well established in both experimental (Rubatto and Hermann, 2007) and high-grade metamorphic rock systems (Buick et al., 2006; Harley, 2001; Hermann and Rubatto, 2003; Kelly and Harley, 2005; Rubatto and Hermann, 2003; Rubatto, 2002; Rubatto et al., 2006). The ability to examine the timing of zircon growth with respect to the growth of a petrologically sensitive mineral such as garnet can greatly improve the veracity of the interpreted *P-T-t* evolution of rock systems. This is particularly relevant to high-grade metamorphic terranes where the timing of zircon growth may not necessarily record the timing of peak metamorphism (Fraser et al., 1997; Kelsey et al., 2008). Although there is still some debate as to the most appropriate HREE distribution coefficients for application to these systems (Buick et al., 2006; Kelly and Harley, 2005; Rubatto, 2002; Rubatto and Hermann, 2007; Rubatto et al., 2006) this technique can be readily applied to the rocks of the PCSS.

One feature is immediately apparent when looking at the HREE and Y profiles across the garnet (Fig 4a), that there is a zone of low HREE and Y abundance that corresponds with the core of the garnet and it is mantled by a strongly enriched zone that then decreases rimward. This profile is interpreted to reflect two stages of garnet growth separated by a period of garnet breakdown and the development of a HREE and Y annulus that separates the core from the rim of the garnet. The interpretation of two stages of garnet growth is consistent with the petrographic observation that the garnet has an inclusion rich core and an inclusion free rim.

When relating the timing of zircon growth relative to that of the silicate mineral assemblage it is useful to establish whether the zircon grew in equilibrium with garnet (e.g. Hermann and Rubatto, 2003; Rubatto, 2002; Rubatto and Hermann, 2003; Whitehouse and Platt, 2003). From the normalised patterns presented in Fig 4c it can be seen that both zircon and garnet display flat to slightly negative Gd to Lu slopes consistent with equilibrium growth. However, when the D_{REE}(zrc/grt) studies of previous workers from natural rock samples (Fig 7a) and experimental studies (Fig.7b) (Harley et al., 2001; Whitehouse and Platt, 2001; Rubatto, 2002; Rubatto and Hermann, 2007; Taylor and Harley, unpubl. data) are compared to the relative abundances of MREE and HREE in the garnet and zircon of this study it is apparent that the zircon analysed was not in equilibrium with garnet of any composition in sample I05-54, regardless of which D_{REE}(zrc/grt) is used. Calculated D_{REE}(zrc/grt) values decrease slightly from Sm to Gd in all zones of the garnet. The core/rim boundary (CRB) and rim analyses then show a steady decline in D_{REE}(zrc/grt) values from Tb to Lu (CRB: Tb = 2.04 to Lu = 0.44; rim Tb =3.71 to Lu = 1.22), whereas the core shows a slight increase (Tb = 2.69 to Lu = 3.56). These patterns and D_{REE}(zrc/grt) values are siginificantly different when compared to the results from the study of natural studies (Figure 7a). The absolute D_{REE}(zrc/grt) values in the CRB and rim are favoured in zircon over garnet by a factor of 2-3 times the published range in studies from Harley (2001) and Whitehouse and Platt (2001). The study of Rubatto (2002), which yielded different results to the other previous studies, shows a steady increase in D_{REE}(zrc/grt) values from Tb to Lu this is again in contrast to the decrease (CRB and rim) or minor increase (core) observed in this study. When compared to recent experimental studies of zircon-garnet REE partitioning the D_{REE}(zrc/grt) patterns are again inconsistent with the zircon and garnet in sample I05-54 being in equilibrium. Rubatto and Hermann (2007) again show a steady increase in the D_{REE} values from Dy to Lu (Figure 7b). I05-54 also shows the MREEs being favoured in the zircon over garnet by a factor of 2.

A second diagnostic feature recorded by the REE contents of the zircon in sample I05-54 is the lack of a pronounced negative Eu anomaly. This feature suggests that zircon did not growth in the presence of an anatectic melt phase (Hoskin and Schaltegger, 2003). When coupled with the distinctive flat chondrite-normalised HREE profile and high HREE contents relative to garnet these observations suggest that zircon grew during metamorphism, prior to the onset of partial melting and not during the growth of garnet. The flat HREE patterns observe suggest that zircon was competing with another phase that incorporates HREE and as discussed above this phase is unlikely to be garnet. Rare inclusions of xenotime are observed in the garnet rims (Fig. 3g) and this may be competing with zircon resulting in the observed flat HREE patterns in zircon. Xenotime growth could have been the result of apatite and/or monazite breakdown during cooling releasing the required P.

The temperature of zircon growth can be constrained to be between 672-724 °C via the application of the Ti in zircon thermometer (Watson and Harrison, 2005; Watson et al., 2006). The application of this thermometer is dependent upon the growth of zircon in equilibrium with quartz and rutile. The knowledge of the $a TiO_2$ and $a SiO_2$ at the time of zircon growth are fundamental to the accuracy of the Ti in zircon thermometer (Ferry and Watson, 2007). Sample I05-54 contains rutile and quartz suggesting that there is potential for the application of the Ti in zircon thermometer.

Rutile occurs as inclusions in the same phases as zircon and seems to be in textural equilibrium with zircon suggesting $aTiO_2$ = 1. However, quartz only occurs in the inclusion assemblage and is not necessarily in equilibrium with zircon and rutile. As previously discussed, zircon growth occurs prior to partial melting and this is suggestive of the growth of zircon in a rock that has not undergone modification of it's bulk composition due to the loss of partial melt. We therefore contend that quartz was likely to be part of the assemblage ($aSiO_2$ = 1) during zircon growth and the Ti in zircon thermometer being applicable in this case.

Monazite chemistry

Less is understood about the relationship of monazite growth to major silicate mineral phases, especially during high-grade metamorphic events such as those experienced by the samples used in this study (Kelsey et al., 2008). The occurrence of large monazite grains restricted to the symplectitic overgrowths on the coarse garnet and kyanite assemblage suggests a relationship between symplectite formation and monazite growth. However this observation alone is not enough to conclude that the monazite ages from this study constrain the timing of symplectite formation. The chondrite normalised REE patterns in sample I05-54 have a pronounced negative Eu anomaly. A negative Eu anomaly in these rocks could be generated in a couple of ways, monazite could inherit the negative Eu anomaly from the source rocks, or form from a rock composition that has undergone partial melting where Eu^{2+} has been incorporated into plagioclase in place of Ca (e.g. Nagy et al., 2002). The presence of a negative Eu anomaly is a common feature of monazite in high-grade metamorphic rocks that have undergone partial melting (e.g. Bea and Montero, 1999; Buick et al., 2006; Hermann and Rubatto, 2003; Rubatto et al., 2006) and in the case of monazite in sample I05-54 the partial melting process is the most likely mechanism to generate the observed Eu anomaly. Partial melting is preferred to the inheritance of the REE pattern from the host rock because no negative Eu anomaly is recorded in the zircon and garnet from the sample, which would be expected if the original host rock had a negative Eu anomaly (e.g. Schulz et al., 2006).

A composite P-T evolution of PCSS

It is difficult to reconstruct the early prograde path of the rocks from the Panangad area but some first order observations can be made based on the petrographic evidence preserved as inclusions in the porphyroblastic garnet and the trace element zoning of the garnet. The early prograde evolution of sample I05-54 led to the formation of the inclusion assemblage of gedrite-sillimanite-quartz possibly in equilibrium with garnet. It is near impossible to constrain the bulk rock chemistry relevant for the inclusion assemblage as it has been substantially modified by partial melting and associated melt-loss. This makes the calculation of a P-T pseudosection for this early evolution quite difficult to do and therefore quantitative P-T constraints on this early assemblage nearly impossible to reconstruct. However, the inclusion assemblage of gedrite-sillimanite-quartz ± garnet suggest the initial prograde path experienced by I05-54 did not exceed temperatures greater than 700-780 °C as the prograde FMASH gedrite + garnet = cordierite + orthopyroxene reaction was not crossed (grey shaded area on Fig. 8a; Diener et al., 2008). The presence of sillimanite also places an upper pressure limit of 8 kbars on the inclusion assemblage.

Sample I05-54 developed the coarse-grained mineral assemblage garnet-kyanite-biotite subsequent to the formation of the inclusion assemblage. The formation of this assemblage was most likely related to the formation of the Y annulus in the garnet that represents a period of garnet breakdown and Y resorption by the garnet. To achieve the garnet breakdown and the formation of kyanite in sample I05-54 would either have to move up pressure or down temperature from the conditions experienced during the inclusion assemblage formation. An up-pressure evolution, while consistent with the formation of kyanite, is inconsistent with the breakdown of garnet and generation of the observed Y annulus. For this reason we prefer an episode of cooling subsequent to the formation of the gedrite-sillimanite-quartz-garnet assemblage. The breakdown of garnet during this cooling event would liberate zirconium (e.g. Degeling et al., 2001; Fraser et al., 1997) and trigger the sub-solidus growth of zircon. The chemistry of zircon analysed in this study is consistent with this scenario for two reasons. Firstly, the D_{REE}(zrc/grt) of the sample indicates that zircon and garnet did not grow in equilibrium. Secondly, the Ti in zircon thermometer indicates that metamorphic zircon grew at temperatures between 672-724 °C, consistent with cooling from the conditions related to the growth of gedrite-sillimanite-quartz-garnet.

After cooling, I05-54 underwent a period of reheating that drove the rock through the solidus resulting in partial melting, melt loss and the generation and preservation of the coarse grained mineral assemblages, symplectite and the growth of monazite. A metamorphic forward model for a specific rock bulk compositions (*P-T* pseudosection) is presented in Figures 8b. Figure 8b was calculated from a composition determined by XRF analysis of sample I05-54. The *P-T* pseudosection was calculated using THERMOCALC v3.31i (Powell and Holland, 1988). The K_2O-FeO-MgO-Al_2O_3-SiO_2-H_2O (KFMASH) including the minerals garnet (g) (Holland and Powell, 1998), orthopyroxene (opx) (Powell and Holland, 1999), cordierite (cd) (Holland and Powell, 1998), spinel (sp), aluminosilicate (and/ky/sill), biotite (bi) (White et al., 2007), K-feldspar (ksp), quartz (q), sapphirine (sa) (Kelsey et al., 2004; White et al., 2001), osumilite (osm) (Holland et al., 1996), corundum (crn), silicate liquid (liq) (White et al., 2007) and H_2O-fluid the pseudosection was calculated using the 5.5s update to enable the incorporation of sapphirine into the model (Kelsey et al., 2004).

The pseudosection shown in Figure 8b constrains the peak conditions experienced at this time from the symplectite assemblage cordierite-sapphirine-spinel-garnet-sillimanite-melt that are ~ 7.5 kbar and 920 °C (Fig. 7b). The reheating is consistent with the growth of a second stage of inclusion-free garnet and subsequent decompression to form the cordierite-sapphirine-spinel symplectites and the related growth of monazite. The presence of the negative Eu anomaly displayed by the monazite is consistent with growth from a partially melted rock, the Eu being removed from the bulk rock composition via the removal of plagioclase, during high-grade metamorphism (e.g. Buick et al., 2006; Rubatto et al., 2006).

A regional tectonic scenario

The mineral parageneses outlined above describes an initial prograde evolution that generated the gedrite-sillimanite-quartz-garnet assemblage, which was followed by a period of cooling, garnet resorption, and kyanite and zircon growth at ~535 Ma. A subsequent episode of heating (second stage garnet growth), followed by decompression (symplectite formation and monazite growth) occurred at ~525 Ma.

This sequence of events is consistent with the initial thickening of a hot crust (Fig. 9a) that is then subsequently cooled towards a normal geotherm (Fig. 9b). Cooling is then followed by crustal thickening and an up-pressure evolution (Fig. 9c). A second thermal pulse, approximately 10 Ma later, heats the crust to ~920 °C and is associated with decompression (Fig. 9d). We interpret this second heating/decompression pulse to be due to delamination of the sub-continental lithospheric mantle after continental collision. This is consistent with reflection seismic images that show a shallowing in Moho depth beneath the PCSS (Rajendra-Prasad et al. 2006).

Such a scenario of repeated pulsative heating and cooling related to extensional and contractional events on a subduction margin (tectonic switching) has been previously proposed for the generation of granulite terranes on an evolving collisional continental margin (Collins, 2002a; Collins, 2002b) in both ancient (Lachlan and New England Orogens, Australia) and modern (Taupo Vocanic Zone, New Zealand) settings. In this scenario, transient rollback of a subducting slab induces extension in the overriding plate and the formation of back-arc basins and the production and emplacement of basaltic magmas via advection from the decompressed asthenosphere resulting in thermally anomalous crustal conditions. The arrival of more buoyant oceanic plateaus induces a period of flat subduction that drives compression focussed into the thermally softened back arc and the formation of a narrow hot orogenic belt (Collins, 2002a). A back-arc setting for metamorphism associated with the PCSS is consistent with recent observations made by Brown (2006; 2007) who suggests that Ediacaran-Cambrian (Pan-African) mobile belts show similarities to inverted, thickened back-arc basins. With the high heat flow at these sites (Hyndman et al., 2005) being able to account for the generation of the observed UHT mineral assemblages in the inverted and eroded back-arc settings.

The tectonic switching model of Collins (2002a) is consistent with a number of first order observations about the setting of the PCSS: 1) The PCSS is situated close to the continental margin during the Neoproterozoic amalgamation of Gondwana (Collins and Pisarevsky, 2005); 2) there is a two stage heating process; the first of which is associated with crustal thickening and is separated from the second by a stage of cooling, the second thermal pulse being related to delamination of the lithospheric mantle and upwelling asthenosphere; 3) The rate of this change in subduction style in eastern Australia has been proposed to be in the order of ~10 Ma, this is consistent with the age data of the cooling and reheating events presented in this paper. Previous workers have interpreted the PCSS as a suture zone between Neoproterozoic India and Azania (Collins et al., 2007b; Shimpo et al., 2006; Santosh et al., 2009). We concur that the PCSS was proximal to an Ediacaran-Cambrian active margin, but suggest that data presented here are consistent with the Panangad being the northern part of the Madurai Block (Fig. 1)—a part of the Neoproterozoic continent Azania—to the present day south of the proposed suture zone within a continental back-arc setting.

Summary

The coupled accessory phase, major silicate mineral parageneses, trace element geochemistry, geochronology and *P-T* pseudosections presented in this paper allow a relatively complete *P-T-t* evolution and tectonic setting for the rocks of the PCSS to be deduced.

1. HREE data from zircon is consistent with zircon growth during the breakdown of garnet at between 672-755 °C in the kyanite stability field at 535.0 ± 4.9 Ma.

2. Monazite growth and symplectite formation occured at 920 °C and 7.5 kbar, ~10 Ma after zircon growth and reflects a period of reheating and decompression related to delamination. The REE chemistry of the monazite is consistent with the rock having undergone partial melting prior to monazite growth, thereby altering the bulk rock chemistry.

3. The periodicity of the heating and cooling cycles (~10 Ma) from this study are consistent with recently proposed tectonic switching models for the formation of granulite metamorphism in accretionary/collisional tectonic settings (Collins, 2002a). The elevated heat flows required to generate the UHT metamorphism are achievable in the proposed back-arc setting for the Pannangad locality within the PCSS during Gondwana amalgamation (e.g. Brown, 2007; Hyndman et al., 2005).

References

Bartlett J. M., Dougherty-Page J. S., Harris N. B. W., Hawkesworth C. J., Santosh M., 1998. The application of single zircon evaporation and model Nd ages to the interpretation of polymetamorphic terrains: an example from the Proterozoic mobile belt of south India. Contributions to Mineralogy and Petrology. 131, 181-195

Bea F., Montero P., 1999. Behavior of accessory phases and redistribution of Zr, REE, Y, Th, and U during metamorphism and partial melting of metapelites in the lower crust: An example from the Kinzigite Formation of Ivrea-Verbano, NW Italy. Geochimica et Cosmochimica Acta. 63, 1133-1153

Bhaskar Rao Y. J., Chetty T. R. K., Janardhan A. S., Gopalan K., 1996. Sm-Nd and Rb-Sr ages and P-T history of the Archean Sittampundi and Bhavani layered meta-anorthosite complexes in Cauvery shear zone, South India: evidence for Neoproterozoic reworking of Archean crust. Contributions to Mineralogy and Petrology. 125, 237-250

Bhaskar Rao Y. J., Janardhan A. S., Vijaya Kumar T., Narayana B. L., Dayal A. M., Taylor P. N., Chetty T. R. K., 2003. Sm-Nd Model Ages and Rb-Sr Isotopic Systematics of Charnockites and Gneisses across the Cauvery Shear Zone, Southern India: Implications for the Archaean - Neoproterozoic Terrane Boundary in the Southern Granulite Terrain. Memoir Geological Society of India. 50, 297-317

Boger S. D., Miller J. M., 2004. Terminal suturing of Gondwana and the onset of the Ross-Delamerian Orogeny: the cause and effect of an Early Cambrian reconfiguration of plate motions. Earth and Planetary Science Letters. 219, 35-48

Boger S. D., Wilson C. J. L., 2005. Early Cambrian crustal shortening and a clockwise P-T-t path from the southern Prince Charles Mountains, East Antarctica: implications for the formation of Gondwana. Journal of Metamorphic Geology. 23, 603-623

Brown M., 2006. Duality of thermal regimes is the distinctive characteristic of plate tectonics since the Neoarchean. Geology. 34, 961-964

Brown M., 2007. Metamorphic conditions in orogenic belts: A record of secular change. International Geology Review. 49, 193-234

Buick I. S., Hermann J., Williams I. S., Gibson R. L., Rubatto D., 2006. A SHRIMP U-Pb and LA-ICP-MS trace element study of the petrogenesis of garnet-cordierite-orthoamphibole gneisses from the Central Zone of the Limpopo Belt, South Africa. Lithos. 88, 150-172

Chetty T. R. K., Bhaskar Rao Y. J., 2006. The Cauvery Shear Zone, Southern Granulite Terrain, India: A crustal-scale flower structure. Gondwana Research. 10, 77-85

Chetty T. R. K., Bhaskar Rao Y. J., Narayana B. L., 2003. A Structural cross section along Krishnagiri-Palani Corridor, Southern Granulite Terrain of India. Memoir Geological Society of India. 50, 255-277

Clark, C., Collins, A.S., Kinny, P.D., Timms, N.E., Chetty, T.R.K., 2008 SHRIMP U-Pb age constraints on the age of charnockite magmatism and metamorphism in the Salem Block, southern India. Gondwana Research. doi: 10.1016/j.gr.2008.11.001

Clark, C., Hand, M., Kelsey, D.E., Goscombe, B., 2007. Linking crustal reworking to terrane accretion. Journal of the Geological Society, London. 164, 937-940

Collins A. S., 2006. Madagascar and the amalgamation of Central Gondwana. Gondwana Research. 9, 3-16

Collins, A.S., Santosh, M., Braun, I., Clark, C., 2007a. Age and sedimentary provenance of the Southern Granulites, South India. U-Th-Pb SHRIMP secondary ion mass spectrometry. Precambrian Research. 155, 125-138.

Collins A. S., Clark C., Sajeev K., Santosh M., Kelsey D. E., Hand M., 2007b. Passage through India: the Mozambique Ocean suture, high-pressure granulites and the Palghat-Cauvery shear zone system. Terra Nova. 19, 141-147

Collins A. S., Pisarevsky S. A., 2005. Amalgamating eastern Gondwana: The evolution of the Circum-Indian Orogens. Earth-Science Reviews. 71, 229-270

Collins A. S., Windley B. F., 2002. The tectonic evolution of central and northern Madagascar and its place in the final assembly of Gondwana. Journal of Geology. 110, 325-339

Collins W. J., 2002a. Hot orogens, tectonic switching, and creation of continental crust. Geology. 30, 535-538

Collins W. J., 2002b. Nature of extensional accretionary orogens. Tectonics. 21, Corfu F., Hanchar J. M., Hoskin P. W. O., Kinny P. D., 2003. Atlas of zircon textures. In: Hanchar J. M., Hoskin P. W. O. (eds) Zircon, vol 53. Mineralogical Society of America, Reviews in Mineralogy and Geochemistry, Washington, D.C., pp 468-500

Degeling H., Eggins S., Ellis D. J., 2001. Zr budgets for metamorphic reactions, and the formation of zircon from garnet breakdown. Mineralogical Magazine. 65, 749-758

Diener J. F. A., Powell R., White R. W., Holland T. J. B., 2007. A new thermodynamic model for clino- and orthoamphiboles in the system Na_2O-CaO-FeO-M_gO-Al_2O_3-SiO_2-H_2O-O. Journal of Metamorphic Geology. 25, 631-656

Drury S. A., Harris N. B. W., Holt R. W., Reeves-Smith G. W., Wightman R. T., 1984. Precambrian tectonics and crustal evolutionin south India. Journal of Geology. 92, 1-20

Drury S. A., Holt R. W., 1980. The tectonic framework of the south Indian craton: A reconnaissance involving Landsat imagery. Tectonophysics. 65, T1-T15

Fitzsimons I. C. W., 2000. A Review of tectonic events in the East Antarctic Shield and their implications for Gondwana and earlier supercontinents. Journal of African Earth Sciences. 31, 3-23

Fraser G., Ellis D., Eggins S., 1997. Zirconium abundance in granulite-facies minerals, with implications for zircon geochronology in high-grade rocks. Geology. 27, 607-610

Ghosh J. G., de Wit M. J., Zartman R. E., 2004. Age and tectonic evolution of Neoproterozoic ductile shear zones in the Southern Granulite Terrain of India, with implications for Gondwana studies. Tectonics. 23,

Harley S. L., 1998a. On the occurrence and characterization of ultrahigh-temperature metamorphism. In: Treloar P. J., O'Brien P. J. (eds) What Drives Metamorphism and Metamorphic Reactions?, vol 138. Geological Society of London, pp 81-107

Harley S. L., 1998b. Ultrahigh temperature granulite metamorphism (1050 degrees C, 12 kbar) and decompression in garnet (Mg70)-orthopyroxene-sillimanite gneisses from the Rauer Group, East Antarctica. Journal of Metamorphic Geology. 16, 541-562

Harley S. L., 2004. Extending our understanding of Ultrahigh temperature crustal metamorphism. Journal of Mineralogical and Petrological Sciences. 99, 140-158

Harley S. L., Kelly N. M., 2007. The impact of zircon-garnet REE distribution data on the interpretation of zircon U-Pb ages in complex high-grade terrains: An example from the Rauer Islands, East Antarctica. Chemical Geology. 241, 62-87

Harley S. L., Kelly N. M., Moller A., 2007. Zircon behaviour and the thermal histories of mountain chains. Elements. 3, 25-30

Harris N. B. W., Santosh M., Taylor P. N., 1994b. Crustal Evolution in South India: Constraints from Nd Isotopes. The Journal of Geology. 102, 139-150

Hermann J., Rubatto D., 2003. Relating zircon and monazite domains to garnet growth zones: age and duration of granulite facies metamorphism in the Val Malenco lower crust. Journal of Metamorphic Geology. 21, 833-852

Holland T. J. B., Babu E., Waters D. J., 1996. Phase relations of osumilite and dehydration melting in pelitic rocks: A simple thermodynamic model for the KFMASH system. Contributions to Mineralogy and Petrology. 124, 383-394

Holland T. J. B., Powell R., 1998. An internally consistent thermodynamic data set for phases of petrological interest. Journal of Metamorphic Geology. 16, 309-343

Hoskin P. W. O., Schaltegger U., 2003. The composition of zircon and igneous and metamorphic petrogenesis. In: Hanchar J. M., Hoskin P. W. O. (eds) Zircon, vol. Mineralogical Society of America, Reviews in Mineralogy & Geochemistry, Volume 53, Washington, D.C., pp 27-62

Hyndman R. D., Currie C. A., Mazzotti S., 2005. Subduction zone backarcs, mobile belts, and orogenic heat. GSA Today. 15, 4-10

Kanazawa, T., Tsunogae, T., Sato, K. & Santosh, M. 2009. The stability and origin of sodicgedrite in ultrahigh-temperature Mg-Al granulites: a case study from the Gondwana suture in southern India. Contributions to Mineralogy and Petrology. 157, 95-110.

Kelly N. M., Harley S. L., 2005. An integrated microtextural and chemical approach to zircon geochronology: refining the Archaean history of the Napier Complex, east Antarctica. Contributions to Mineralogy and Petrology. 149, 57-84

Kelsey, D.E., Clark, C., Hand, M., 2008. Thermobarometric modeling of zircon and monazite growth in melt bearing systems. Journal of Metamorphic Geology. 26, 199-212.

Kelsey D. E., Clark C., Hand M., Collins A. S., 2006. Comment on "First report of garnet-corundum rocks from southern India: Implications for prograde high-pressure (eclogite-facies?) metamorphism". Earth and Planetary Science Letters. 249, 529-534.

Kelsey D. E., Hand M., Clark C., Wilson C. J. L., 2007. On the application of in situ monazite chemical geochronology to constraining P-T-t histories in high-temperature (> 850 degrees C polymetamorphic granulites from Prydz Bay, East Antarctica. Journal of the Geological Society. 164, 667-683.

Kelsey D. E., White R. W., Holland T. J. B., Powell R., 2004. Calculated phase equilibria in K_2O-FeO-MgO-Al_2O_3-SiO_2-H_2O for sapphirine-quartz-bearing mineral assemblages. Journal of Metamorphic Geology. 22, 559-578.

Koshimoto S., Tsunogae T., Santosh M., 2004. Sapphirine and corundum bearing ultrahigh temperature rocks from the Palghat-Cauvery Shear System, southern India. Journal of Mineralogical and Petrological Sciences. 99, 298-310.

Li Z. X., Bogdanova S. V., Collins A. S., Davidson A., De Waele B., Ernst R. E., Fitzsimons I. C. W., Fuck R. A., Gladkochub D. P., Jacobs J., Karlstrom K. E., Lu S., Natapov L. M., Pease V., Pisarevsky S. A., Thrane K., Vernikovsky V., In Press. Assembly, configuration, and break-up history of Rodinia: A synthesis. Precambrian Research. 160, 179-210.

Meert J. G., 2003. A synopsis of events related to the assembly of eastern Gondwana. Tectonophysics. 362, 1-40

Meert J. G., Van der Voo R., 1997. The Assembly of Gondwana 800-550 Ma. Journal of Geodynamics. 23, 223-235

Meissner B., Deters P., Srikantappa C., Kohler H., 2002. Geochronological evolution of the Moyar, Bhavani and Palghat shear zones of southern India: implications for east Gondwana correlations. Precambrian Research. 114, 149-175

Nagy G., Draganits E., Demeny A., Panto G., Arkai P., 2002. Genesis and transformations of monazite, florencite and rhabdophane during medium grade metamorphism: examples from the Sopron Hills, Eastern Alps. Chemical Geology. 191, 25-46

Payne, J., Hand M., Barovich K., Wade B. P., 2008. Temporal constraints on the timing of high-grade metamorphism in the northern Gawler Craton:

implications for assembly of the Australian Proterozoic. Australian Journal of Earth Sciences. 55, 623-640.
Pearce N. J. G., Perkins W. T., Westgate J. A., Gorton M. P., Jackson S. E., Neal C. R., Chenery S. P., 1997. A compilation of new and published major and trace element data for NIST SRM 610 and NIST SRM 612 glass reference materials. Geostandards Newsletter-the Journal of Geostandards and Geoanalysis. 21, 115-144
Powell R., Holland T. J. B., 1988. An internally consistent thermodynamic dataset with uncertainties and correlations: 3. Applications to geobarometry, worked examples and a computer program. J. Metamorphic Geol. 6, 173-204
Powell R., Holland T. J. B., 1999. Relating formulations of the thermodynamics of mineral solid solutions: activity modelling of pyroxenes, amphiboles and micas. American Mineralogist. 84,
Reeves C., de Wit M. J., 2000. Making ends meet in Gondwana: retracing the transforms of the Indian Ocean and reconnecting continental shear zones. Terra Nova. 12, 272-280
Roberts M. P., Finger F., 1997. Do U-Pb zircon ages from granulites reflect peak metamorphic conditions? Geology. 25, 319-322
Rubatto D., 2002. Zircon trace element geochemistry: partitioning with garnet and the link between U-Pb ages and metamorphism. Chemical Geology. 184, 123-138
Rubatto D., Hermann J., 2003. Zircon formation during fluid circulation in eclogites (Monviso, Western Alps): Implications for Zr and Hf budget in subduction zones. Geochimica et Cosmochimica Acta. 67, 2173-2187
Rubatto D., Hermann J., 2007. Experimental zircon/melt and zircon/garnet trace element partitioning and implications for the geochronology of crustal rocks. Chemical Geology. 241, 38-61
Rubatto D., Hermann J., Buick I. S., 2006. Temperature and bulk composition control on the growth of monazite and zircon during low-pressure anatexis (Mount Stafford, central Australia). Journal of Petrology. 47, 1973-1996
Rubatto D., Williams I. S., Buick I. S., 2001. Zircon and monazite response to prograde metamorphism in the Reynolds Range, central Australia. Contributions to Mineralogy and Petrology. 140, 458-468.

Santosh, M., Maruyama, S. & Sato, K. 2009. Anatomy of a Cambrian suture in Gondwana: Pacific type orogeny in southern India? Gondwana Reseach doi: 10.1016/j.gr.2008.12.012.

Santosh M., Sajeev K., 2006. Anticlockwise evolution of ultrahigh-temperature granulites within continental collision zone in southern India. Lithos. 92, 447-464

Santosh M., Tanaka K., Yokoyama K., Collins A. S., 2005. Late Neoproterozoic-Cambrian felsic magmatism along transcrustal shear zones in southern India: U-Pb electron microprobe ages and implications for the amalgamation of the Gondwana supercontinent. Gondwana Research. 8, 31-42

Santosh M., Tsunogae T., Koshimoto S., 2004. First report of sapphirine-bearing rocks from the Palghat-Cauvery Shear Zone System, southern India. Gondwana Research. 7, 620-626

Santosh M., Yokoyama K., Biju-Sekhar S., Rogers J. J. W., 2003. Mutiple tectonothermal events in the granulite blocks of southern India revealed from EPMA dating: implications on the history of supercontinents. Gondwana Research. 6, 29-63

Schulz B., Klemd R., Bratz H., 2006. Host rock compositional controls on zircon trace element signatures in metabasites from the Austroalpine basement. Geochimica Et Cosmochimica Acta. 70, 697-710

Shaju K. M., Yoshida M., Santosh M., 1998. Shear Zones of Southern India: Implications for the Proterozoic Tectonics of East Gondwana. Gondwana Research. 1, 420-421

Shimpo M., Tsunogae T., Santosh M., 2006. First report of garnet-corundum rocks from southern India: Implications for prograde high-pressure (eclogite-facies?) metamorphism. Earth and Planetary Science Letters. 242, 111-129

Tomkins H. S., Williams I. S., Ellis D. J., 2005. In situ U-Pb dating of zircon formed from retrograde garnet breakdown during decompression in Rogaland, SW Norway. Journal of Metamorphic Geology. 23, 201-215

Tomson J. K., Bhaskar Rao Y. J., Vijaya Kumar T., Mallikharjuna Rao J., 2006. Charnockite genesis across the Archaean-Proterozoic terrane boundary in the South Indian Granulite Terrain: Constraints from major-trace element geochemistry and Sr-Nd isotopic systematics. Gondwana Research. 10, 115-127

Tsunogae T., Santosh M., 2006. Reply to Comment on "First report of garnet-corundum rocks from southern India: Implications for prograde high-pressure (eclogite-facies?) metamorphism" by D.E. Kelsey, C. Clark, M. Hand, A.S. Collins. Earth and Planetary Science Letters. 249, 535-540

Van Achterbergh E., Ryan C. G., Jackson S. E., Griffin W. L., 2001. Data reduction software for LA-ICP-MS. In: Sylvester Paul J. (ed) Laser-ablation-ICPMS in the earth sciences; principles and applications., vol. Mineralogical Association of Canada. Ottawa, ON, Canada. 2001.,

Watson E. B., Harrison T. M., 2005. Zircon thermometer reveals minimum melting conditions on earliest Earth. Science. 308, 841-844

Watson E. B., Wark D. A., Thomas J. B., 2006. Crystallization thermometers for zircon and rutile. Contributions to Mineralogy and Petrology. 151, 413-433

White R. W., Powell R., 2002. Melt loss and the preservation of granulite facies mineral assemblages. Journal of Metamorphic Geology. 20, 621-632

White R. W., Powell R., Clarke G. L., 2002. The interpretation of reaction textures in Fe-rich metapelitic granulites of the Musgrave Block, central Australia: constraints from mineral equilibria calculations in the system K_2O-FeO-MgO-Al_2O_3-SiO_2-H_2O-TiO_2-Fe_2O_3. Journal of Metamorphic Geology. 20, 41-55

White R. W., Powell R., Halpin J. A., 2004. Spatially-focussed melt formation in aluminous metapelites from Broken Hill, Australia. Journal of Metamorphic Geology. 22, 825-845

White R. W., Powell R., Holland T. J. B., 2001. Calculation of partial melting equilibria in the system Na_2O-CaO-K_2O-FeO-MgO-Al_2O_3-SiO_2-H_2O (NCKFMASH). Journal of Metamorphic Geology. 19, 139-153

White R. W., Powell R., Holland T. J. B., 2007. Progress relating to calculation of partial melting equilibria for metapelite. Journal of Metamorphic Geology. 25, 511-527

White R. W., Powell R., Holland T. J. B., Worley B., 2000. The effect of TiO_2 and Fe_2O_3 on metapelitic assemblages at greenschist and amphibolite facies conditions: mineral equilibria calculations in the system K_2O-FeO-MgO-Al_2O_3-SiO_2-H_2O-TiO_2-Fe_2O_3. Journal of Metamorphic Geology. 18, 497-511

Whitehouse M. J., Platt J. P., 2003. Dating high-grade metamorphism - constraints from rare-earth elements in zircon and garnet. Contributions to Mineralogy and Petrology. 145, 61-74

Williams I. S., Claesson S., 1987. Isotopic evidence for the Precambrian provenance and Caledonian metamorphism of high grade paragneisses from the Seve Nappes, Scandinavian Caledonides. Contributions to Mineralogy and Petrology. 97, 205-217

Figure Captions

Figure 1 – (a) Map of southern Indai showing the various protolith ages amd major structural features. (b) Enlargement of area in (a) showing the location of the Panangad sample area.

Figure 2 – (a) Field photograph of a garnet-kyanite-biotite gneiss with kyanite blades aligned in the shear plane. Scale bar has 1 cm increments. (b) Field photo of garnet-kyanite-biotite gneiss (1cm increment on scale bar). (c) Photomicrograph of garnet separated form biotite by a narrow rim of cordierite, and the development of a sapphirine + cordierite symplectite between the garnet and coarse grained kyanite. The pits from the LA-ICPMS traverse are visible running vertically through the garnet (field of view = 8000 μm) (d) Sapphirine + cordierite and sapphirine +spinel symplecties separating kyanite (partially pseudomorphed by sillimanite) and garnet. Note the monazite in the symplectite (field of view = 3500 μm). (e) Gedrite + sillimanite + quartz inclusion in garnet. (f) Zircon and rutile in coarse grained kyanite blades. (g) Sapphirine-cordierite and spinel-cordierite symplectites between garnet and kyanite porphyroblasts with cordierite separating garnet from sapphirine and spinel. (h) Fine grained biotite in cordierite, note the monazite in the reaction texture and the zircon in the kyanite. (i) monazite intergrown with a sapphirine-cordierite symplectite.

Figure 3 – (a-g) Electron probe maps of garnet with characteristic retrograde zoning pattern, LA-ICPMS analysis spots marked. Location of the electron microprobe spot analysis traverse across the garnet shown in part (4a) is shown on (b).

Figure 4 – major and trace element data for garnet. (a) Electron microprobe spot analysis traverse across the garnet (b) LA-ICPMS traverse for Lu, Yb and Y as shown in Fig. 3a. (c) Chondrite normalised rare earth element patterns for the core, intermediate and rim of the garnet.

Figure 5 – (a-d) CL images of zircons showing main textural features. (e) Wetherill concordia plot of U-Pb analyses from sample I05-54 (after Collins et al., 2007). (f) Range of temperatures obtained from Ti in zircon thermometry. Chondrite normalise REE patterns for (g) older oscillatory zoned cores and (h) zircon rims and new grown metamorphic zircon.

Figure 6 – (a) BSE images of a selection of analysed monazites showing main textural features and the location of U-Pb spot analyses. (b) Wetherill concordia plot of U-Pb monazite data from monazite cores for sample I05-54. (c) Wetherill concordia plot of U-Pb monazite data from monazite rims for sample I05-54. (d) Chondrite normalised REE patterns for monazite.

Figure 7 – Comparison of the REE distribution patterns between zircon and garnet in (a) natural samples and (b) experimental studies. (Rubatto'02 = Rubatto

(02); W & P '03=Whitehouse and Platt 2003; Harley UHT '01 = Harley, 2001; RH07 = Rubatto and Hermann, 2007).

Figure 8 – (a) Schematic phase diagram showing possible maximum temperatures and pressure experienced during the early metamorphic evolution of sample I05-54. The oam + grt = crd + opx FMASH reaction line is from Diener et al., 2008). (b) Pseduosections calculated for a bulk composition determined by XRF analysis of sample I05-54. Bulk rock compositions are in molecular weight percent.

Figure 9 – Cartoon showing the tectonic evolution of the region around the PCSS from immediately prior to collision of the Dharwar craton at 540 Ma and final amalgamation at 525 Ma.

Table Captions

Table 1 – Electron microprobe garnet compositions.

Table 2 - Spinel, sapphirine gedrite, cordierite, and two generations of biotite electron microprobe compositions.

Table 3 –U-Pb monazite age data from LA-ICPMS.

Table 4 – LA-ICPMS garnet trace element compositions.

Table 5 – LA-ICPMS zircon trace element compositions and Ti in zircon thermometry.

Table 6 – LA-ICPMS monazite trace element compositions

All Figures

Figure 1

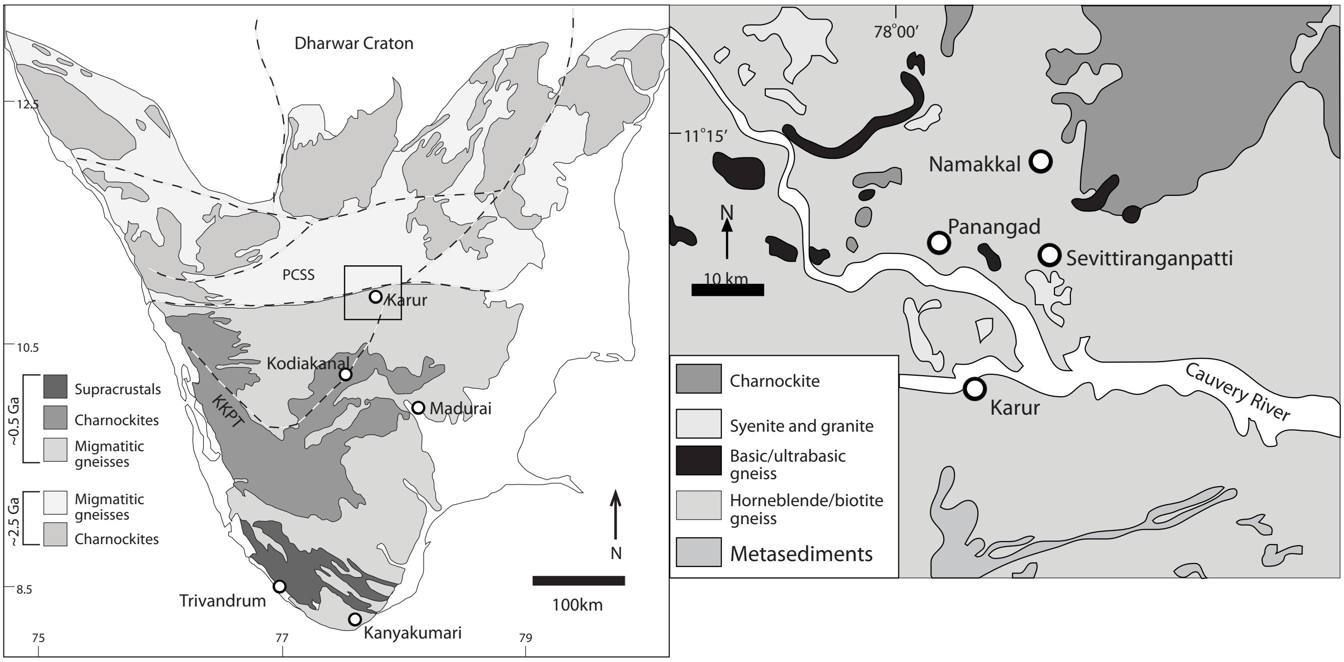

Figure 2

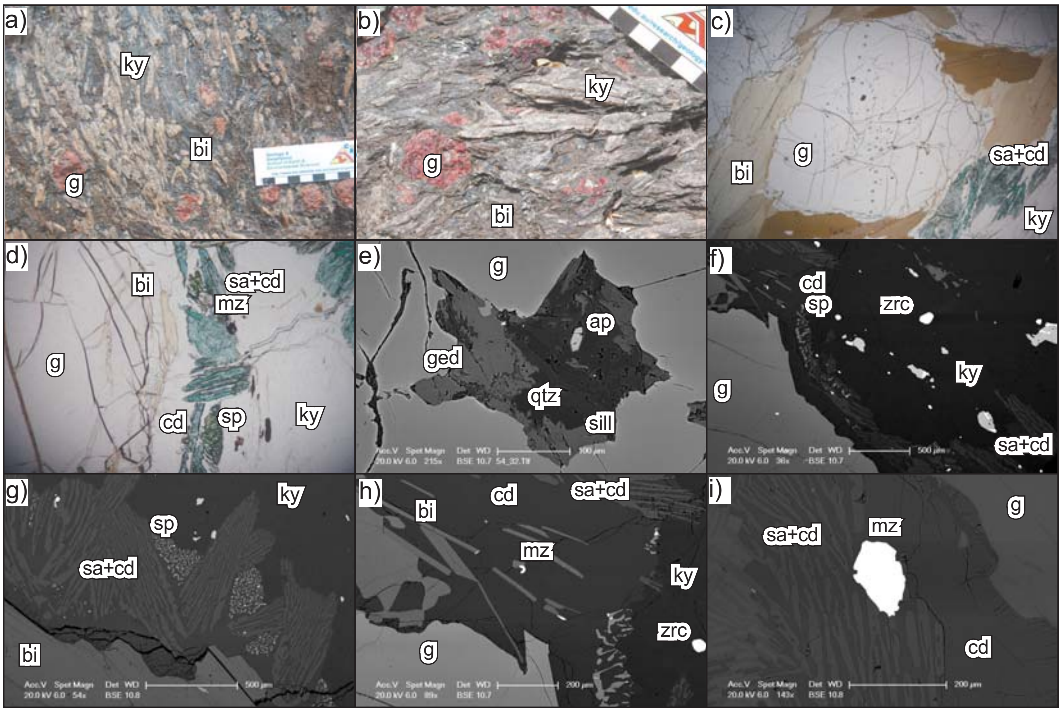
a)
ky
bi
g
b)
ky
g
bi
c)
g
bi
sa+cd
ky
d)
bi
sa+cd
mz
g
cd
sp
ky
e)
g
ap
ged
qtz
sill
f)
cd
sp
zrc
ky
g
sa+cd
g)
ky
sp
sa+cd
bi
h)
bi
cd
sa+cd
mz
ky
zrc
g
i)
sa+cd
mz
g
cd

Figure 3

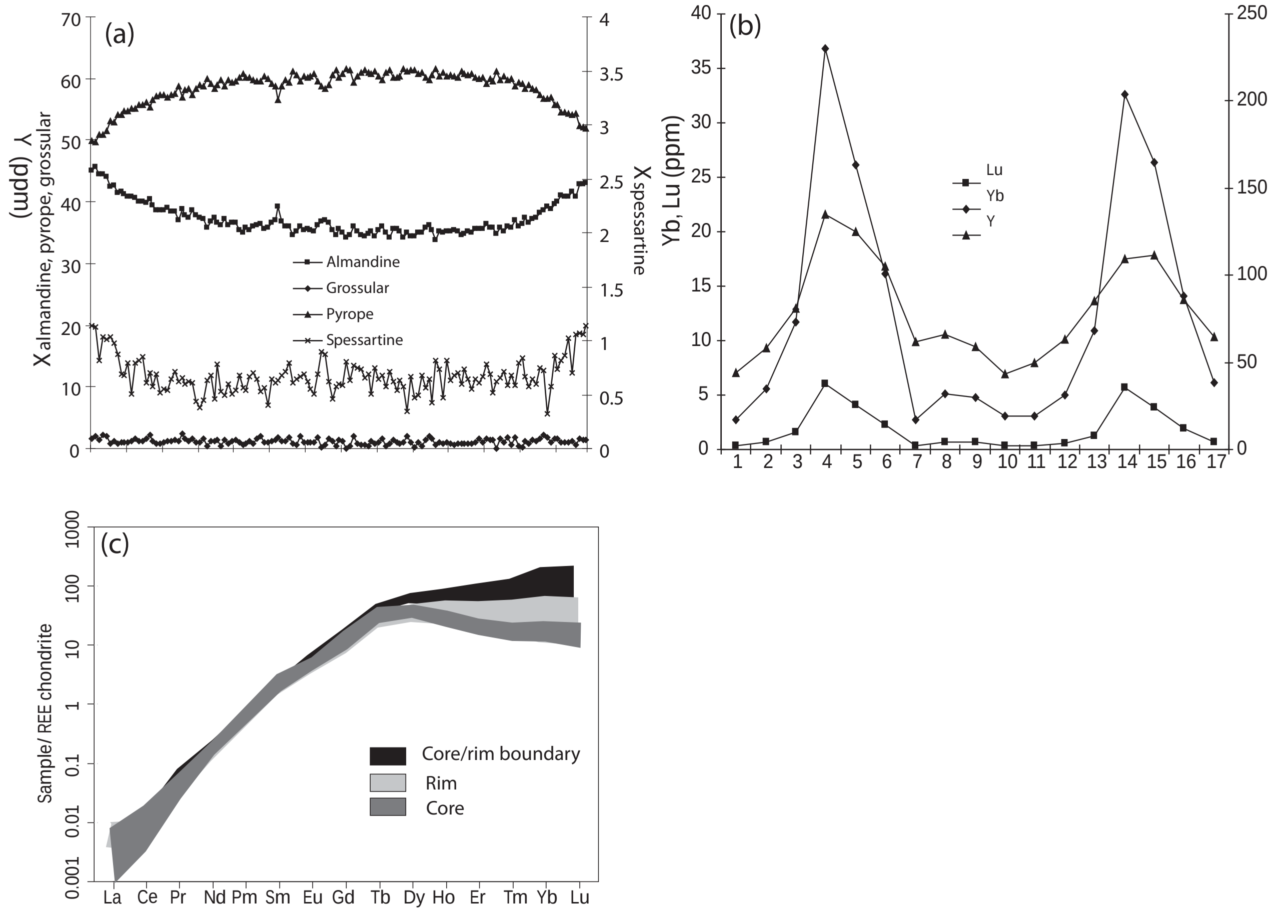

(a)
X almandine, pyrope, grossular
Y (ppm)
X spessartine
Almandine
Grossular
Pyrope
Spessartine
(b)
Yb, Lu (ppm)
Lu
Yb
Y
(c)
Sample/ REE chondrite
Core/rim boundary
Rim
Core
La Ce Pr Nd Pm Sm Eu Gd Tb Dy Ho Er Tm Yb Lu

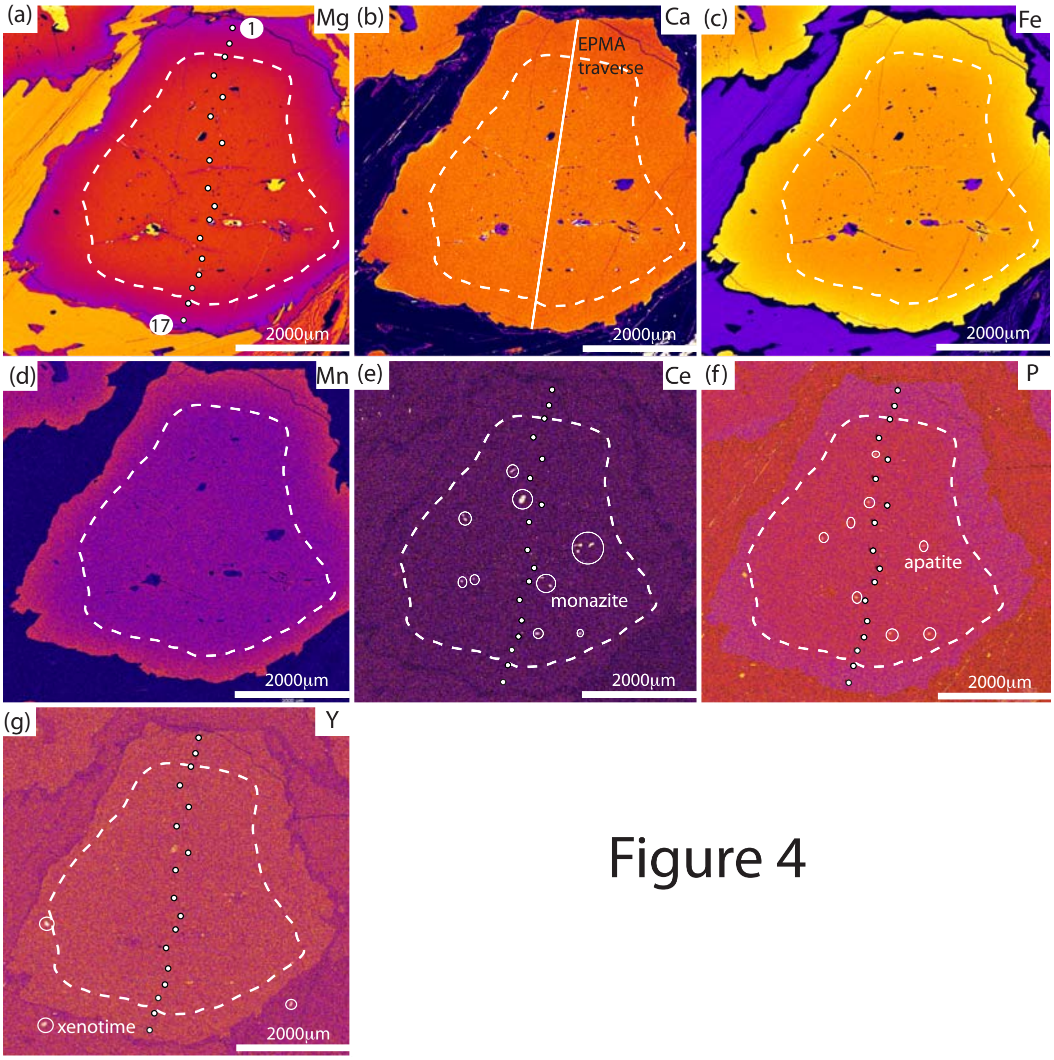

(a)
Mg
1
17
2000μm
(b)
Ca
EPMA traverse
2000μm
(c)
Fe
2000μm
(d)
Mn
2000μm
(e)
Ce
monazite
2000μm
(f)
P
apatite
2000μm
(g)
Y
xenotime
2000μm

Figure 4

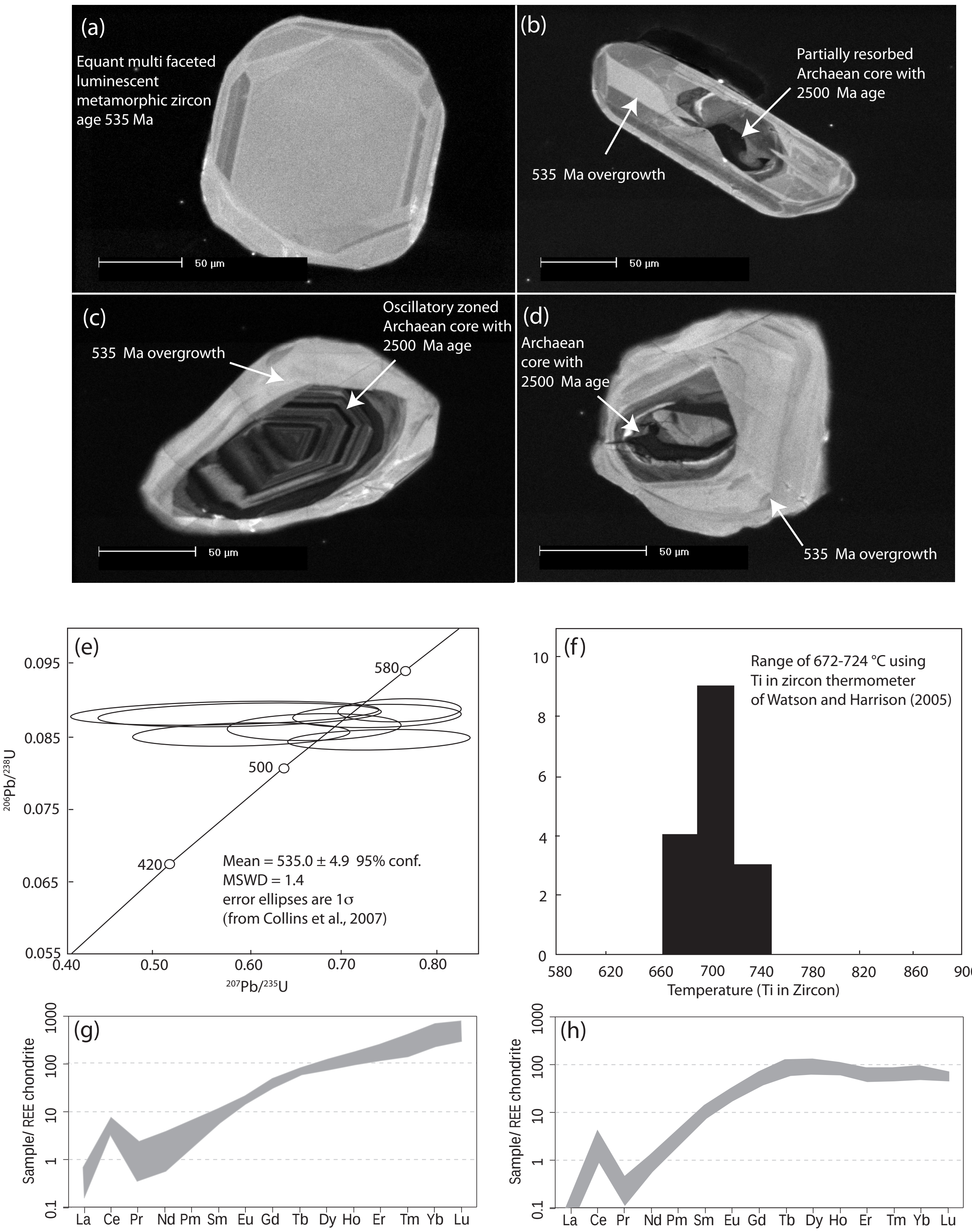

(a)
Equant multi faceted luminescent metamorphic zircon age 535 Ma
50 µm
(b)
Partially resorbed Archaean core with 2500 Ma age
535 Ma overgrowth
50 µm
(c)
535 Ma overgrowth
Oscillatory zoned Archaean core with 2500 Ma age
50 µm
(d)
Archaean core with 2500 Ma age
535 Ma overgrowth
50 µm
(e)
580
500
420
Mean = 535.0 ± 4.9 95% conf.
MSWD = 1.4
error ellipses are 1σ
(from Collins et al., 2007)
206Pb/238U
207Pb/235U
0.095
0.085
0.075
0.065
0.055
0.40
0.50
0.60
0.70
0.80
(f)
Range of 672-724 °C using Ti in zircon thermometer of Watson and Harrison (2005)
Temperature (Ti in Zircon)
0
2
4
6
8
10
580
620
660
700
740
780
820
860
900
(g)
Sample/ REE chondrite
0.1
1
10
100
1000
La Ce Pr Nd Pm Sm Eu Gd Tb Dy Ho Er Tm Yb Lu
(h)
Sample/ REE chondrite
0.1
1
10
100
1000
La Ce Pr Nd Pm Sm Eu Gd Tb Dy Ho Er Tm Yb Lu

Figure 5

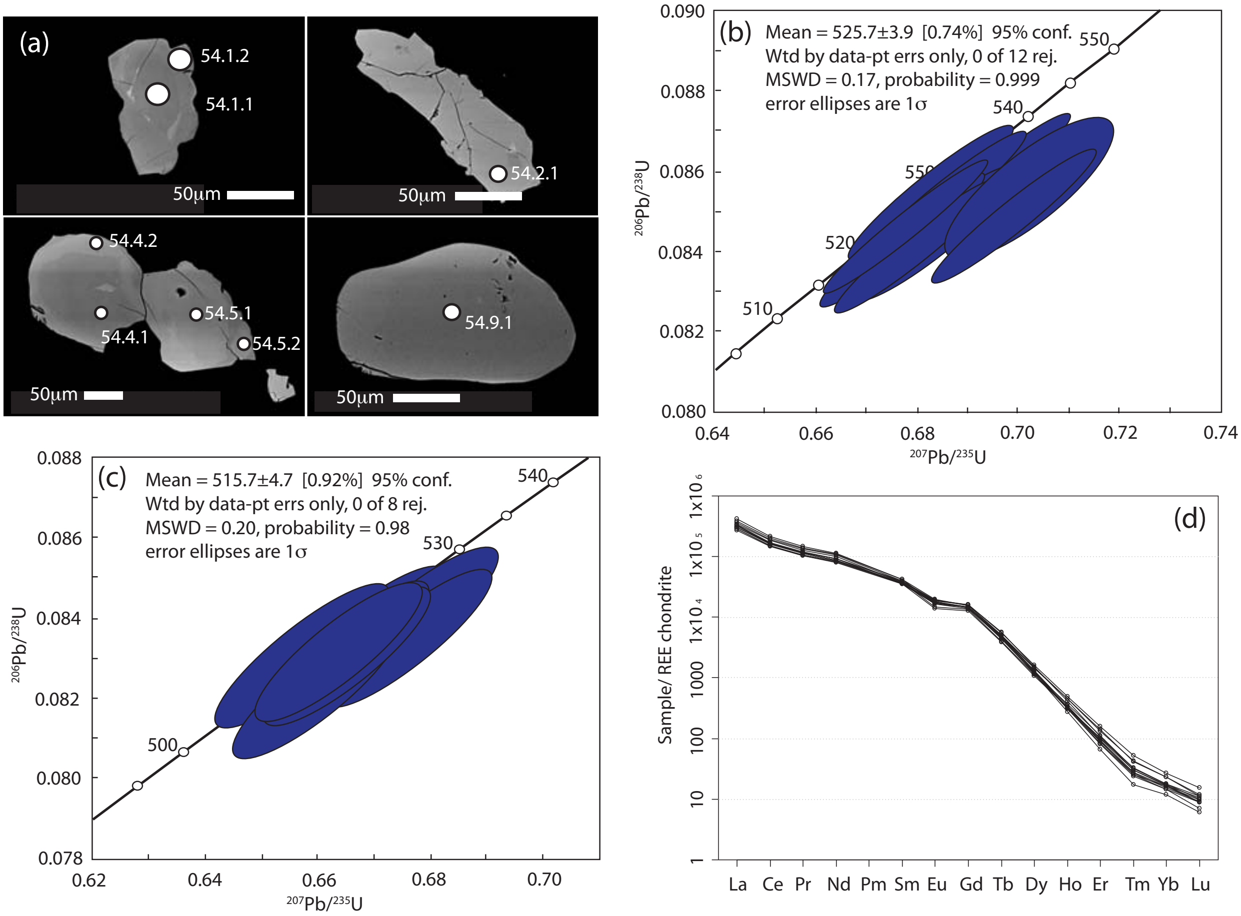

(a)
54.1.2
54.1.1
54.2.1
54.4.2
54.4.1
54.5.1
54.5.2
54.9.1
50µm
(b)
Mean = 525.7±3.9 [0.74%] 95% conf.
Wtd by data-pt errs only, 0 of 12 rej.
MSWD = 0.17, probability = 0.999
error ellipses are 1σ
550
540
520
510
0.090
0.088
0.086
0.084
0.082
0.080
0.64
0.66
0.68
0.70
0.72
0.74
206Pb/238U
207Pb/235U
(c)
Mean = 515.7±4.7 [0.92%] 95% conf.
Wtd by data-pt errs only, 0 of 8 rej.
MSWD = 0.20, probability = 0.98
error ellipses are 1σ
540
530
500
0.088
0.086
0.084
0.082
0.080
0.078
0.62
0.64
0.66
0.68
0.70
206Pb/238U
207Pb/235U
(d)
Sample/ REE chondrite
1x10 6
1x10 5
1x10 4
1000
100
10
1
La Ce Pr Nd Pm Sm Eu Gd Tb Dy Ho Er Tm Yb Lu

Figure 6

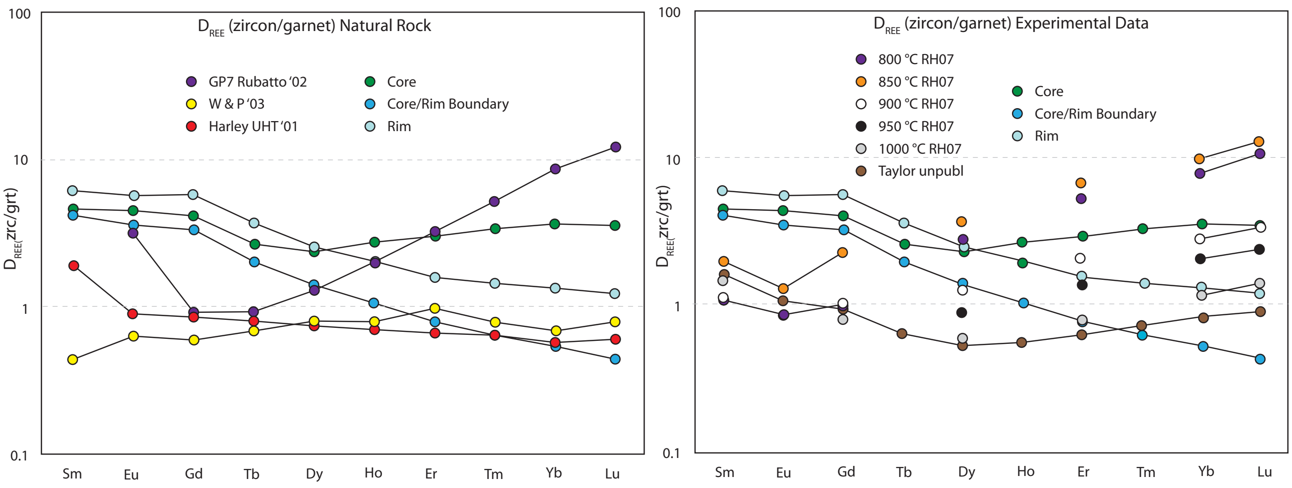

D_REE (zircon/garnet) Natural Rock
GP7 Rubatto '02
W & P '03
Harley UHT '01
Core
Core/Rim Boundary
Rim
D_REE zrc/grt)
100
10
1
0.1
Sm
Eu
Gd
Tb
Dy
Ho
Er
Tm
Yb
Lu
D_REE (zircon/garnet) Experimental Data
800 °C RH07
850 °C RH07
900 °C RH07
950 °C RH07
1000 °C RH07
Taylor unpubl
Core
Core/Rim Boundary
Rim

Figure 7

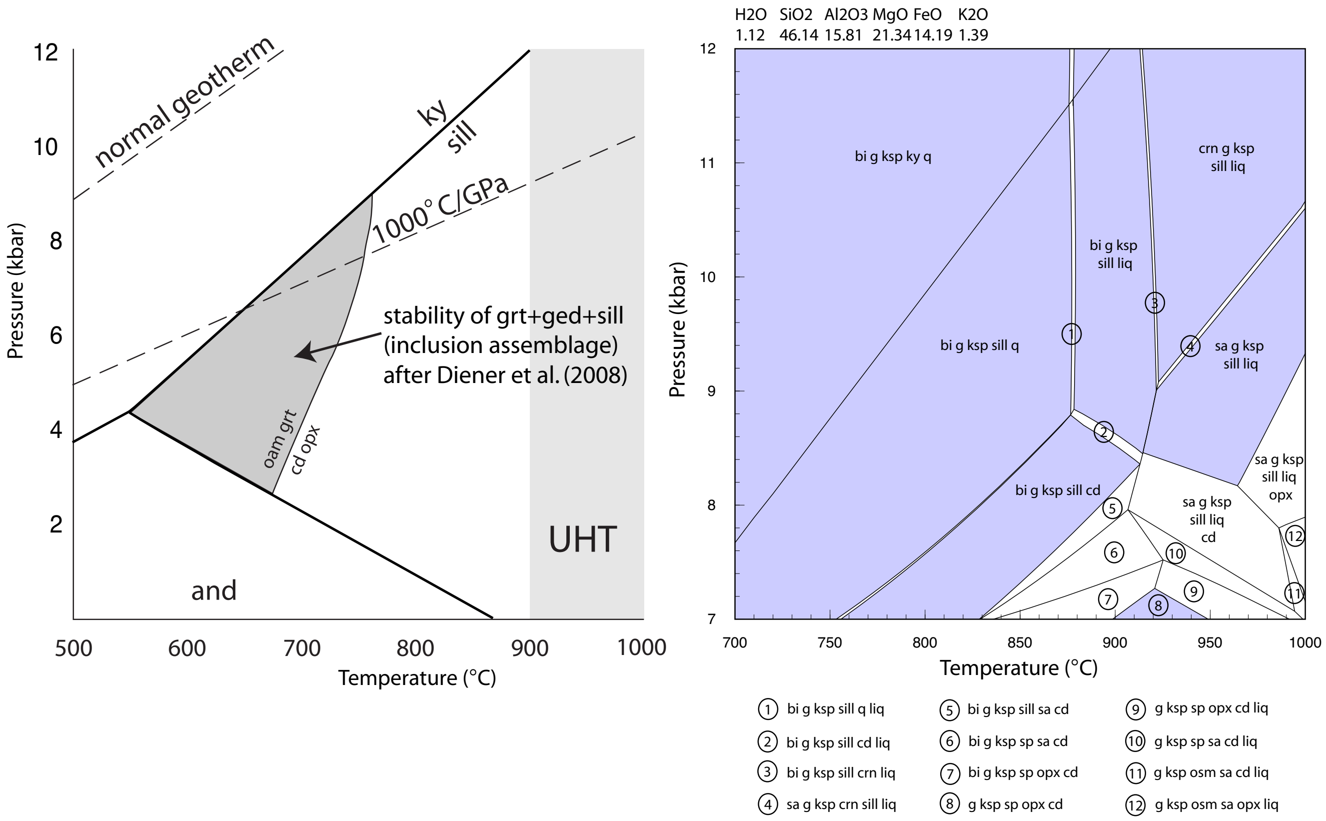

normal geotherm
ky
sill
1000° C/GPa
stability of grt+ged+sill
(inclusion assemblage)
after Diener et al. (2008)
oam grt
cd opx
UHT
and
Pressure (kbar)
Temperature (°C)
H2O SiO2 Al2O3 MgO FeO K2O
1.12 46.14 15.81 21.34 14.19 1.39
bi g ksp ky q
crn g ksp sill liq
bi g ksp sill liq
bi g ksp sill q
sa g ksp sill liq
sa g ksp sill liq opx
bi g ksp sill cd
sa g ksp sill liq cd
Pressure (kbar)
Temperature (°C)
1 bi g ksp sill q liq
2 bi g ksp sill cd liq
3 bi g ksp sill crn liq
4 sa g ksp crn sill liq
5 bi g ksp sill sa cd
6 bi g ksp sp sa cd
7 bi g ksp sp opx cd
8 g ksp sp opx cd
9 g ksp sp opx cd liq
10 g ksp sp sa cd liq
11 g ksp osm sa cd liq
12 g ksp osm sa opx liq

Figure 8

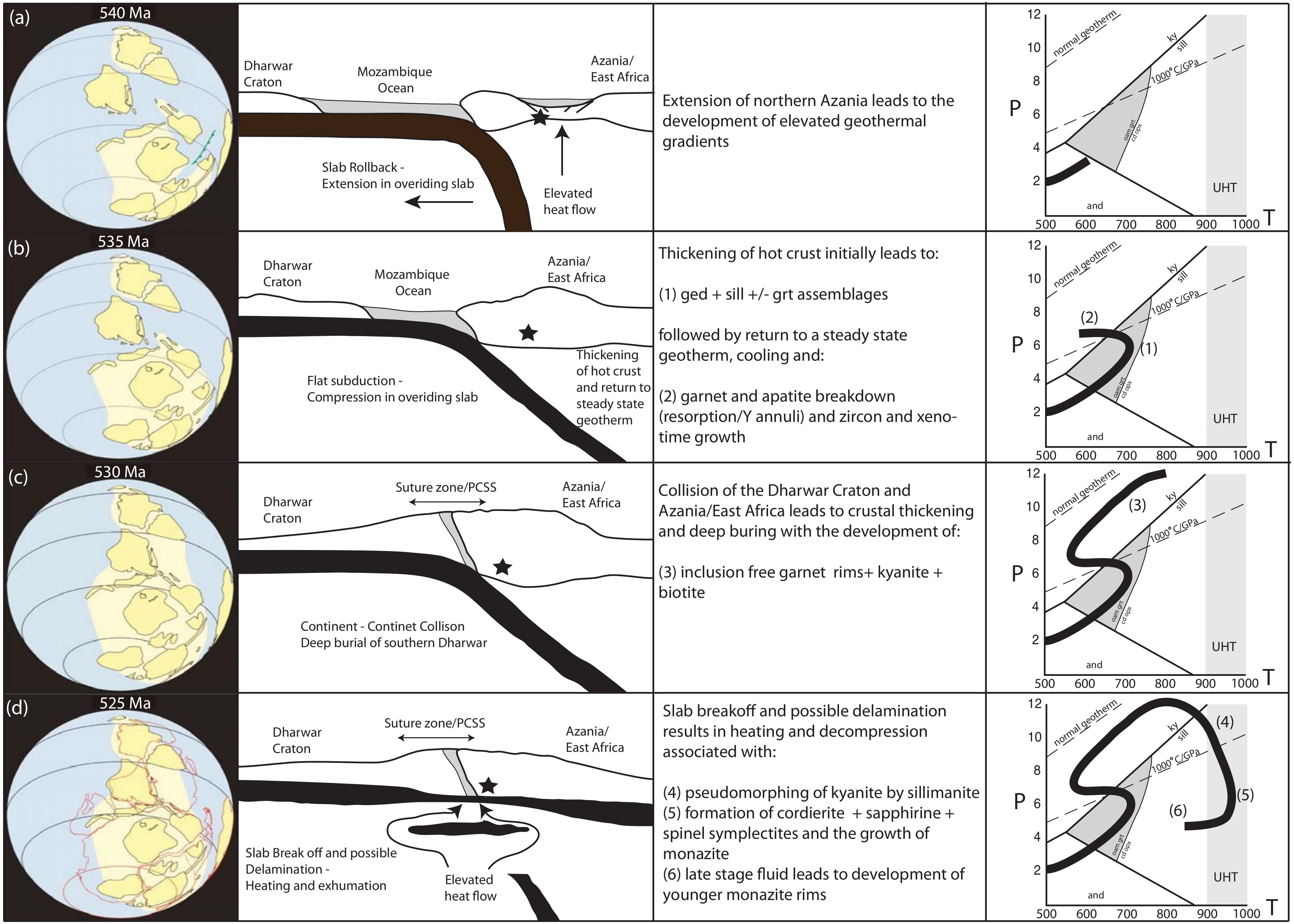

(a)
540 Ma
Dharwar Craton
Mozambique Ocean
Azania/ East Africa
Slab Rollback - Extension in overiding slab
Elevated heat flow
Extension of northern Azania leads to the development of elevated geothermal gradients
(b)
535 Ma
Dharwar Craton
Mozambique Ocean
Azania/ East Africa
Flat subduction - Compression in overiding slab
Thickening of hot crust and return to steady state geotherm
Thickening of hot crust initially leads to:
(1) ged + sill +/- grt assemblages
followed by return to a steady state geotherm, cooling and:
(2) garnet and apatite breakdown (resorption/Y annuli) and zircon and xeno-time growth
(c)
530 Ma
Dharwar Craton
Suture zone/PCSS
Azania/ East Africa
Continent - Continet Collison Deep burial of southern Dharwar
Collision of the Dharwar Craton and Azania/East Africa leads to crustal thickening and deep buring with the development of:
(3) inclusion free garnet rims+ kyanite + biotite
(d)
525 Ma
Dharwar Craton
Suture zone/PCSS
Azania/ East Africa
Slab Break off and possible Delamination - Heating and exhumation
Elevated heat flow
Slab breakoff and possible delamination results in heating and decompression associated with:
(4) pseudomorphing of kyanite by sillimanite
(5) formation of cordierite + sapphirine + spinel symplectites and the growth of monazite
(6) late stage fluid leads to development of younger monazite rims
P
T
normal geotherm
ky
sill
1000° C/GPa
oam grt
cd opx
and
UHT
500 600 700 800 900 1000
2 4 6 8 10 12

Table 1

TABLE 1: EPMA major element analyses of garnet

	Rim				Core				Rim			
	Gt-6	Gt-9	Gt-11	Gt-13	Gt-35	Gt-36	Gt-37	Gt-39	Gt-135	Gt-136	Gt-137	Gt-138
SiO_2	39.54	39.42	39.48	39.81	40.17	40.04	39.80	39.94	39.70	39.31	39.86	39.77
TiO_2	0.00	0.12	0.01	0.00	0.00	0.04	0.01	0.04	0.04	0.00	0.03	0.04
Al_2O_3	22.53	22.63	22.66	22.75	22.58	22.87	22.85	22.95	22.62	22.74	22.65	22.58
Fe_2O_3	0.88	0.86	0.93	0.65	0.93	0.78	1.08	0.97	0.78	1.03	0.76	0.86
FeO	21.38	21.17	20.84	20.47	18.99	18.83	19.02	18.95	20.98	21.18	21.53	21.61
MnO	0.48	0.32	0.37	0.37	0.22	0.37	0.25	0.28	0.33	0.49	0.50	0.50
MgO	14.10	14.32	14.50	14.74	15.72	15.84	15.94	15.99	14.44	14.34	14.00	13.91
CaO	1.26	1.30	1.36	1.26	1.40	1.34	1.32	1.34	1.27	1.34	1.37	1.45
Total	100.17	100.12	100.14	100.05	100.01	100.10	100.28	100.46	100.16	100.43	100.70	100.71
Si	2.96	2.94	2.94	2.96	2.97	2.96	2.94	2.94	2.96	2.93	2.96	2.96
Al^{iv}	0.04	0.06	0.06	0.04	0.03	0.04	0.06	0.06	0.04	0.07	0.04	0.04
Al^{vi}	1.94	1.94	1.94	1.96	1.94	1.95	1.93	1.94	1.95	1.94	1.95	1.94
Ti	0.00	0.01	0.00	0.00	0.00	0.00	0.00	0.00	0.00	0.00	0.00	0.00
Fe^{3+}	0.05	0.05	0.05	0.04	0.05	0.04	0.06	0.05	0.04	0.06	0.04	0.05
Fe^{2+}	1.34	1.32	1.30	1.27	1.17	1.16	1.17	1.17	1.31	1.32	1.34	1.34
Mn	0.03	0.02	0.02	0.02	0.01	0.02	0.02	0.02	0.02	0.03	0.03	0.03
Mg	1.57	1.59	1.61	1.63	1.73	1.74	1.75	1.75	1.60	1.59	1.55	1.54
Ca	0.10	0.10	0.11	0.10	0.11	0.11	0.10	0.11	0.10	0.11	0.11	0.12
Total	8.03	8.03	8.04	8.03	8.02	8.03	8.04	8.04	8.03	8.05	8.03	8.03
X_{Alm}	42.41	41.64	40.78	40.63	37.47	36.68	36.21	36.14	41.67	40.92	42.88	42.90
X_{Grs}	0.89	1.07	1.03	1.52	1.15	1.38	0.50	0.84	1.21	0.68	1.54	1.46
X_{Pyr}	53.15	54.15	54.74	55.20	58.32	58.97	59.70	59.67	54.21	54.39	52.36	52.14
X_{Spss}	1.03	0.69	0.79	0.79	0.46	0.78	0.53	0.60	0.70	1.05	1.07	1.06

Table 2

TABLE 2: EPMA major element analyses of spinel, sapphirine, gedrite, cordierite and biotite

	Spinel			Sapphirine			Gedrite			Cordierite			Biotite (coarse)			Biotite (fine)		
SiO_2	0.12	0.08	0.10	12.20	12.24	12.02	44.14	44.49	44.28	50.56	50.58	50.63	38.50	38.28	37.92	38.42	38.44	38.29
TiO_2	0.02	0.00	0.00	0.03	0.02	0.06	0.44	0.43	0.38	0.00	0.01	0.00	1.95	2.01	2.15	2.00	1.97	1.94
Al_2O_3	61.41	61.02	60.51	62.07	62.23	62.48	19.16	19.12	19.19	33.20	32.97	32.92	17.35	17.58	17.75	17.84	17.79	17.71
Cr_2O_3	0.41	0.33	0.42	0.19	0.21	0.24	0.07	0.08	0.06	0.00	0.00	0.00	0.13	0.06	0.06	0.09	0.09	0.02
FeO	24.38	24.72	24.77	8.85	9.07	8.80	10.68	10.39	10.19	2.67	2.44	2.42	8.58	8.79	8.67	8.67	8.52	8.63
MnO	0.06	0.00	0.05	0.05	0.01	0.04	0.01	0.00	0.06	0.08	0.00	0.08	0.00	0.03	0.00	0.04	0.02	0.00
MgO	12.48	12.11	12.24	16.56	16.72	16.36	21.51	21.89	22.16	12.80	12.79	12.91	19.56	19.70	19.73	19.74	19.68	19.50
ZnO	1.18	0.87	0.99	0.04	0.00	0.00	0.00	0.06	0.08	0.05	0.00	0.00	0.02	0.04	0.09	0.08	0.00	0.00
CaO	0.00	0.00	0.00	0.02	0.00	0.00	0.62	0.61	0.56	0.05	0.04	0.04	0.01	0.01	0.00	0.00	0.00	0.00
Na_2O	0.01	0.03	0.00	0.00	0.00	0.04	1.48	1.46	1.62	0.27	0.30	0.20	0.75	0.71	0.79	0.68	0.71	0.73
K_2O	0.00	0.00	0.01	0.00	0.00	0.00	0.01	0.00	0.01	0.00	0.00	0.01	8.51	8.37	8.47	8.45	8.41	8.62
Total	100.08	99.16	99.08	100.02	100.50	100.05	98.12	98.53	98.59	99.68	99.14	99.22	95.37	95.58	95.64	96.00	95.61	95.43
Si	0.00	0.00	0.00	1.47	1.46	1.44	6.12	6.13	6.10	5.01	5.03	5.03	2.76	2.74	2.72	2.74	2.75	2.75
Ti	0.00	0.00	0.00	0.00	0.00	0.01	0.05	0.04	0.04	0.00	0.00	0.00	0.11	0.11	0.12	0.11	0.11	0.10
Al	1.94	1.95	1.94	8.78	8.77	8.83	3.13	3.10	3.12	3.88	3.87	3.86	1.47	1.48	1.50	1.50	1.50	1.50
Cr	0.01	0.01	0.01	0.02	0.02	0.02	0.01	0.01	0.01	0.00	0.00	0.00	0.01	0.00	0.00	0.01	0.00	0.00
Fe^{2+}	0.55	0.56	0.56	0.89	0.91	0.88	1.24	1.20	1.17	0.22	0.20	0.20	0.51	0.53	0.52	0.52	0.51	0.52
Mn^{2+}	0.00	0.00	0.00	0.01	0.00	0.00	0.00	0.00	0.01	0.01	0.00	0.01	0.00	0.00	0.00	0.00	0.00	0.00
Mg	0.50	0.49	0.50	2.96	2.98	2.93	4.44	4.50	4.55	1.89	1.90	1.91	2.09	2.10	2.11	2.10	2.10	2.09
Zn	0.02	0.02	0.02	0.00	0.00	0.00	0.00	0.01	0.01	0.00	0.00	0.00	0.00	0.00	0.00	0.00	0.00	0.00
Ca	0.00	0.00	0.00	0.00	0.00	0.00	0.09	0.09	0.08	0.00	0.00	0.00	0.00	0.00	0.00	0.00	0.00	0.00
Na	0.00	0.00	0.00	0.00	0.00	0.01	0.40	0.39	0.43	0.05	0.06	0.04	0.10	0.10	0.11	0.09	0.10	0.10
K	0.00	0.00	0.00	0.00	0.00	0.00	0.00	0.00	0.00	0.00	0.00	0.00	0.78	0.77	0.78	0.77	0.77	0.79

Table 3

TABLE 3: U-Pb LA-ICP MS Monazite Analyses

Spot No.	$^{206}Pb/^{238}U$	1σ	$^{207}Pb/^{235}U$	1σ	$^{207}Pb/^{206}Pb$	1σ	$^{206}Pb/^{238}U$ (Ma)	1σ	$^{207}Pb/^{235}U$ (Ma)	1σ	$^{207}Pb/^{206}Pb$ (Ma)	1σ	Conc (%)
Core Analyses													
54.1.1	0.08425	0.00114	0.67858	0.00989	0.05831	0.0069	521.4	6.8	525.9	6.0	540.8	26.5	96
54.2.1	0.08438	0.00114	0.67583	0.00982	0.05799	0.0069	522.2	6.8	524.3	6.0	528.8	26.1	99
54.3.1	0.08537	0.00116	0.69674	0.01048	0.05908	0.0074	528.1	6.9	536.8	6.3	570.2	27.0	93
54.4.1	0.08493	0.00115	0.68472	0.00994	0.05836	0.0069	525.5	6.8	529.6	6.0	543.5	25.6	97
54.5.1	0.08450	0.00115	0.68244	0.01015	0.05846	0.0072	522.9	6.8	528.2	6.1	547.2	26.6	96
54.6.1	0.08509	0.00116	0.68995	0.01034	0.0587	0.0073	526.4	6.9	532.8	6.2	556.1	26.9	95
54.7.1	0.08570	0.00116	0.69540	0.01003	0.05874	0.0069	530.1	6.9	536.0	6.0	557.5	25.2	95
54.8.1	0.08462	0.00115	0.68693	0.0099	0.05877	0.0068	523.7	6.8	531.0	6.0	558.5	25.2	94
54.9.1	0.08493	0.00115	0.68741	0.01	0.0586	0.0069	525.5	6.9	531.2	6.0	552.2	25.6	95
54.10.1	0.08544	0.00116	0.68402	0.00993	0.05796	0.0068	528.5	6.9	529.2	6.0	527.9	26.0	100
54.11.1	0.08556	0.00119	0.70125	0.01201	0.05933	0.009	529.2	7.1	539.5	7.2	579.2	32.7	91
54.12.1	0.08526	0.00117	0.69271	0.01049	0.05881	0.0074	527.4	6.9	534.4	6.3	560.2	27.3	94
Rim Analyses													
54.1.2	0.08355	0.00116	0.67464	0.01112	0.05845	0.0084	517.3	6.9	523.5	6.7	546.8	31.1	95
54.3.2	0.08310	0.00114	0.65717	0.01036	0.05725	0.0077	514.6	6.8	512.9	6.4	500.5	29.4	103
54.4.2	0.08311	0.00114	0.67038	0.01046	0.05839	0.0077	514.7	6.8	520.9	6.4	544.4	28.7	95
54.5.2	0.08404	0.00115	0.67645	0.01047	0.05827	0.0076	520.2	6.8	524.6	6.3	539.1	29.0	96
54.8.2	0.08352	0.00115	0.66822	0.01075	0.05792	0.008	517.1	6.9	519.6	6.5	526.4	30.3	98
54.10.2	0.08318	0.00115	0.66830	0.0106	0.05816	0.0079	515.1	6.8	519.7	6.5	535.2	29.9	96
54.11.2	0.08355	0.00116	0.66782	0.01079	0.05786	0.008	517.3	6.9	519.4	6.6	524.4	30.4	99
54.12.2	0.08228	0.00113	0.66079	0.01048	0.05814	0.0079	509.7	6.7	515.1	6.4	534.5	29.9	95

Table 4

TABLE 4: Trace Element LA-ICP MS Garnet Analyses

	G-54.1	G-54.2	G-54.3	G-54.4	G-54.5	G-54.6	G-54.7	G-54.8	G-54.9	G-54.10	G-54.11	G-54.12	G-54.13	G-54.14	G-54.15	G-54.16	G-54.17
Sc	77.37	61.02	82.61	130.94	152.12	157.92	204.57	222.91	219.1	186.43	184.32	176.12	154.66	134.5	118.39	84.06	72.92
Ti	35.41	37.95	42.51	51.88	52.32	50.38	77.2	65.26	73.36	60.05	59.94	52.35	55.21	55.6	53.25	42.33	38.85
P	159.32	169.4	167.69	43.12	46.2	64.18	64.34	58.68	67.71	6.25	4.91	6.86	37.28	55.33	77.68	204.65	266.2
V	23.91	34.18	33.99	36.45	37.69	48.57	73.7	64.55	73.18	63.37	66.72	44.19	47.14	44.31	42.78	34.29	30.43
Cr	233.67	237.42	268.69	232.13	157.33	237.67	259.81	264.12	261.19	256.49	245.99	160.72	167.14	219.62	396.54	238.28	224.29
Y	44.09	58.12	80.99	135.01	124.92	105.36	61.67	65.99	59.06	43.5	50.02	63.52	85.41	109.19	111.33	86.1	64.63
Zr	1.987	2.64	2.17	2.17	2.53	2.58	2.62	2.59	2.36	1.562	1.713	2	2.33	2.54	2.64	2.94	4.22
La	bdl	bdl	0.00125	bdl	bdl	bdl	bdl	bdl	bdl	bdl	0.00027	0.00238	0.0015	bdl	bdl	bdl	0.00283
Ce	0.00335	0.003	0.0048	0.0072	0.0112	0.0127	0.0097	0.0061	0.0094	0.00424	0.00273	0.0146	0.0054	0.0095	0.007	0.0064	0.0078
Pr	0.00327	0.00317	0.00295	0.0047	0.0085	0.0051	0.003	0.0085	0.0082	0.00382	0.00394	0.00482	0.00476	0.0051	0.00444	0.006	0.003
Nd	0.0645	0.0865	0.0738	0.105	0.139	0.135	0.126	0.132	0.14	0.0811	0.0901	0.107	0.104	0.099	0.091	0.09	0.093
Sm	0.278	0.283	0.315	0.379	0.374	0.441	0.502	0.431	0.59	0.317	0.324	0.344	0.398	0.37	0.37	0.313	0.33
Eu	0.237	0.251	0.29	0.387	0.409	0.456	0.401	0.433	0.398	0.286	0.306	0.322	0.354	0.328	0.335	0.301	0.299
Gd	1.752	1.896	2.48	3.44	4.06	3.99	3.76	4.32	3.91	2.39	2.66	3.06	3.23	3.42	3.36	2.72	2.38
Tb	0.858	1.016	1.301	1.99	2.18	2.01	1.98	2.07	1.95	1.173	1.327	1.558	1.743	1.829	1.738	1.327	1.136
Dy	7.83	9.79	13.28	22.12	21.03	19.86	14.9	15.91	14.32	9.85	11.15	14	16.83	19.67	19.25	14.35	11.34
Ho	1.607	2.25	3.42	6.27	5.4	4.6	2.35	2.65	2.29	1.551	1.84	2.49	3.48	5.04	4.92	3.62	2.51
Er	3.59	5.4	9.4	20.02	16.06	11.97	4.19	5.29	4.69	3.26	3.74	5.52	9.08	17.04	16.03	11.03	6.62
Tm	0.456	0.807	1.56	3.9	3.11	2.09	0.517	0.744	0.666	0.405	0.447	0.698	1.386	3.3	2.92	1.741	0.872
Yb	2.71	5.55	11.74	36.84	26.13	16.19	2.75	5.07	4.77	3.1	3.12	4.98	10.88	32.67	26.36	14.07	6.09
Lu	0.306	0.667	1.61	6	4.1	2.22	0.339	0.734	0.699	0.376	0.383	0.582	1.257	5.65	3.89	1.97	0.731
Hf	0.0404	0.0799	0.0579	0.0286	0.017	0.042	0.073	0.039	0.086	0.0281	0.0306	0.0167	0.0388	0.04	0.0548	0.09	0.118

Table 5

TABLE54: Trace element LA-ICP MS Zircon Analyses

	Zr-54.1	Zr-54.2	Zr-54.3	Zr-54.4	Zr-54.5	Zr-54.6	Zr-54.7	Zr-54.8	Zr-54.9	Zr-54.10	Zr-54.11	Zr-54.12
P	191	122	130	130	99	138	119	112	91	110	115	105
Sc	389	380	387	350	320	391	356	350	297	337	303	297
Ti	7.25	8.23	7.52	8.01	5.54	5.78	8.17	7.25	6.31	4.69	4.31	5.58
Y	175	211	215	191	154	179	230	218	179	138	140	142
Nb	0.20	0.17	0.18	0.17	0.16	0.23	0.18	0.16	0.14	0.20	0.17	0.17
La	0.02	0.01	bdl	0.03	0.01	0.01	0.03	bdl	bdl	0.01	0.01	0.02
Ce	2.28	2.09	2.19	2.21	2.02	3.14	2.26	2.21	1.99	2.82	2.34	2.09
Pr	0.03	0.03	0.02	0.04	0.02	0.01	0.03	0.03	0.02	0.02	0.02	0.02
Nd	0.49	0.55	0.45	0.69	0.43	0.45	0.71	0.58	0.49	0.41	0.33	0.37
Sm	1.77	2.28	2.23	2.17	1.60	1.91	2.45	2.31	1.96	1.47	1.46	1.55
Eu	1.64	1.86	1.82	1.77	1.34	1.66	2.09	1.95	1.58	1.17	1.16	1.32
Gd	13.68	16.23	15.75	14.70	12.10	14.64	17.27	16.98	14.32	10.07	10.68	10.97
Tb	4.36	5.42	5.27	4.77	3.88	4.65	5.73	5.46	4.52	3.12	3.41	3.50
Dy	30.99	38.05	37.48	33.93	27.17	31.96	41.09	38.63	32.34	23.48	24.67	25.00
Ho	5.74	6.98	7.19	6.21	5.10	5.93	7.59	7.21	5.92	4.63	4.69	4.72
Er	12.72	15.11	15.98	13.89	11.47	13.47	16.91	16.40	13.33	11.21	10.73	10.69
Tm	1.84	2.24	2.41	2.10	1.73	1.94	2.47	2.29	1.88	1.69	1.63	1.57
Yb	13.21	16.62	17.55	15.76	12.72	14.00	18.24	16.94	13.57	13.42	11.62	11.54
Lu	1.68	2.08	2.23	1.94	1.59	1.67	2.21	2.15	1.73	1.81	1.54	1.51
Hf	13937	13306	13708	12920	12255	15460	13041	13162	11410	13889	12631	12411
Ta	0.04	0.03	0.03	0.04	0.03	0.05	0.02	0.03	0.03	0.04	0.04	0.03
Pb	1.16	0.97	0.95	1.34	1.03	1.51	1.33	1.13	0.94	1.32	1.19	1.29
Zr_{Ti} T	713	724	717	722	692	695	724	713	702	679	672	692
1σ	35	35	35	35	35	35	36	36	36	36	36	36

Table 6

TABLE 6: Trace element LA-ICP MS Monazite Analyses

	M-54.1	M-54.2	M-54.3	M-54.4	M-54.5	M-54.6	M-54.7	M-54.8	M-54.9	M-54.10	M-54.11	M-54.12	M-54.13	M-54.14
P	71750	65621	52106	62048	58773	57812	56277	54493	54515	61437	71810	61160	63109	62134
V	13	13	8	16	15	9	9	9	9	10	16	9	11	7
Y	727	707	521	533	516	515	543	577	481	814	571	506	506	660
Zr	1.60	1.14	0.80	0.94	0.97	0.95	0.81	0.83	0.78	0.87	0.97	0.91	0.86	0.94
Nb	0.05	0.05	0.05	0.05	0.05	0.04	0.05	0.04	0.04	0.04	0.07	0.05	0.05	0.04
La	130242	112049	85354	107435	102530	95897	93651	89586	89533	99458	119703	101497	96844	94296
Ce	176248	156294	119446	148814	138210	132316	129876	124544	121678	135612	162234	132546	132565	129052
Pr	18179	16584	12564	15547	14509	14142	13678	13225	12830	14354	17182	13684	14084	13805
Nd	68609	63411	48120	60368	55897	55154	52506	51537	49547	55271	65990	51800	54712	52517
Sm	8324	7854	6975	7351	6864	7689	7136	7098	7059	7517	8137	6865	7518	7396
Eu	1450	1339	1276	1098	1036	1417	1298	1300	1317	1383	1214	1225	1316	1415
Gd	4033	3816	3836	3468	3282	4105	3850	3874	3756	4136	3806	3583	3852	4144
Tb	236	229	228	190	182	236	228	234	221	261	209	213	227	265
Dy	481	469	397	363	347	399	412	429	377	518	392	382	395	493
Ho	33	32	23	24	23	22	24	25	19	35	26	22	22	29
Er	29	28	18	21	21	17	19	20	14	33	23	17	16	23
Tm	1.35	1.39	0.86	1.05	0.96	0.81	0.81	0.89	0.56	1.70	1.02	0.76	0.69	0.97
Yb	4.79	4.77	3.23	3.68	3.57	3.37	3.05	3.36	2.48	5.64	3.71	3.05	2.93	3.54
Lu	0.38	0.36	0.30	0.31	0.28	0.31	0.28	0.29	0.20	0.49	0.36	0.23	0.27	0.33
Hf	0.46	0.48	0.53	0.49	0.44	0.59	0.48	0.52	0.60	0.51	0.53	0.47	0.49	0.54
Pb	1281	1498	1424	1542	1485	1508	1556	1561	1385	1538	1494	1408	1558	1481